



Delocalization of d-electrons induced by cation coupling in ultrathin Chevrel-phase NiMo_3S_4 nanosheets for efficient electrochemical water splitting

Sundaram Chandrasekaran^{a,b,*}, Tingting Ma^{a,b}, Zhichang Hu^{a,b}, Qianying Liu^{a,b},
Chao Zhan^{a,b}, Yan Li^{a,b}, Chris Bowen^c, Huidan Lu^{a,b,*}, Yongping Liu^{a,b,*}

^a Guangxi Key Laboratory of Electrochemical and Magneto-chemical, Functional Materials, College of Chemistry and Bioengineering, Guilin University of Technology, Guilin 541004, PR China

^b Guangxi Colleges and Universities Key Laboratory of surface and interface electrochemistry, College of Chemistry and Bioengineering, Guilin University of Technology, Guilin 541004, PR China

^c Department of Mechanical Engineering, University of Bath, BA2 7AY Bath, UK

ARTICLE INFO

Keywords:

Chevrel-phase
 NiMo_3S_4
Bifunctional electrocatalysts
d-electron delocalization
HER/OER

ABSTRACT

Chevrel-phase metal sulfides are known to be promising materials for energy conversion and storage applications. However, a detailed understanding of the intrinsic kinetic mechanisms of electrocatalytic bifunctional hydrogen and oxygen evolution reactions (HER/OER) on NiMo_3S_4 -based Chevrel-phases is lacking. Herein, novel ultrathin self-assembled nanosheets of NiMo_3S_4 are coupled with transition metal atoms (M/N- NiMo_3S_4 ; where M = Co, Fe, and Cu) were formed by a facile hydrothermal approach. Notably, the Co/N- NiMo_3S_4 electrocatalyst exhibits excellent performance in terms of ultralow overpotentials of 78, 208, 282, and 307 mV at 10, 100, 500, and 1000 mA cm^{-2} for the HER; and 186, 204, and 225 mV at 50, 100, and 300 mA cm^{-2} for the OER, respectively. Experimental and first principle calculations demonstrate that Co atoms coupling with edge Ni atoms results in d-electron delocalization on Co/N- NiMo_3S_4 , signifying the efficient charge transfer to improve overall water electrolysis. In addition, an upshift in the d-band center of Co/N- NiMo_3S_4 can optimize the free energies of a variety of reaction intermediates for water adsorption and dissociation; thereby facilitating the robust alkaline overall water electrolysis at 1.47 V. This work therefore greatly deepens the understanding of the bifunctional hydrogen and oxygen evolution reaction of Chevrel-phase electrocatalysts.

1. Introduction

In the global mission of achieving carbon neutrality, hydrogen (H_2) generation through water electrolysis is of significant importance. The key reactions involved in water electrolysis include the hydrogen evolution reaction (HER) and oxygen evolution reaction (OER) [1–3]. The application of electrocatalysts to provide excellent activity at high current densities is one potential route for realizing large-scale H_2 production. Currently, the benchmark catalysts are based on precious metals of platinum (Pt) and their alloys for the HER, while the oxides of ruthenium (RuO_2) and iridium (IrO_2) used for the OER [4–7]. Conversely, the scarcity and high cost of precious metals limits their practical applications for large-scale hydrogen (H_2) and oxygen (O_2)

generation. For industrial applications, bifunctional electrocatalysts made of transition metal sulfide active phases dispersed with and without γ -alumina, such as Raney Ni, Ni–Mo–S, and Co–Mo–S have made significant progress for applications related to large-scale alkaline water electrolysis at high current densities of $< 500 \text{ mA cm}^{-2}$. However, due to their relatively poor intrinsic electrocatalytic activity, they require a relatively high cell voltage of 1.6–2.4 V, which greatly surpassed the theoretical thermodynamic water electrolysis potential of 1.23 V [8–12]. As a result, the search for low-cost, highly efficient, and durable non-precious metal-based bifunctional electrocatalysts that operate at a low overpotential remains an area of intense research.

In recent years, researchers have endeavoured to increase the electrocatalytic bifunctional performance of transition metal sulfide-based

* Corresponding authors at: Guangxi Key Laboratory of Electrochemical and Magneto-chemical, Functional Materials, College of Chemistry and Bioengineering, Guilin University of Technology, Guilin 541004, PR China.

E-mail addresses: yes.chandrasekaran@gmail.com, chandru@glut.edu.cn (S. Chandrasekaran), lhuidangl@163.com (H. Lu), liuyup624@163.com (Y. Liu).

<https://doi.org/10.1016/j.apcatb.2023.123007>

Received 28 April 2023; Received in revised form 31 May 2023; Accepted 16 June 2023

Available online 16 June 2023

0926-3373/© 2023 Elsevier B.V. All rights reserved.

materials [13]. Benefiting from the regulated nano-/micro-architecture with rich redox chemistry, exposed active sites, high electrical conductivity, outstanding physical and chemical features, and synergistic coupling effect between two or more metal cations, several transition metal sulfide-based catalysts have been utilized as robust electrocatalysts for bifunctional electrocatalysis; which includes nanosheets of Ni_3S_2 [14], NiS_x [15], $\text{Ru-Ni}_9\text{S}_8$ [16], Fe-MoS_2 [17], $\text{Fe-Ni}_3\text{S}_2$ [18], NiFeS [19], $\text{Fe}_{0.9}\text{Co}_{0.05}\text{S}_{1.05}$ [20], NiCo_2S_4 nanowires [21], $\text{Ni}_{0.33}\text{Co}_{0.67}\text{S}_2$ [22], CoMoS [23], Fe-CoMoS [24], hierarchical CoMoS_3 [25], defect rich NiMo_3S_4 [26], Ni-Fe-Co-S [27], FeCoNiS_x [28] and core-shell FeCo-MoS@NG [29]. Thus, it is believed that transition metal sulfide-based materials can be an alternative choice to accelerate the overall water splitting system and lower the cost of hydrogen production. However, it is still unclear that how metallic dopants affect the electronic structure of such catalysts.

An important family of transition metal sulfides are the Chevrel-phase metal sulfides, $\text{M}^{(\text{II})}\text{Mo}_x\text{S}_{x+1}$, where M is a 3d transition metal or rare earth ion; typically, M is a large cation such as Co, Ni, Fe, Mn, Cu, Cr, Zn, Mg, or Cd [26,30–34]. Initially, Chevrel et al. [35] made significant progress on the fabrication of a variety of Chevrel-phase metal sulfides. To date, the Chevrel-phase sulfides have exhibited versatile chemical properties and are of interest for several fascinating applications, including hydrosulfurization [36], battery electrodes [37], and superconductors [38]. Notably, electrocatalysis of Chevrel-phase NiMo_3S_4 has rarely been researched for either the HER, oxygen reduction reaction (ORR) or OER [39,40]. For example, Jiang et al. [30] prepared a hollow Chevrel-phase nickel molybdenum sulfide (NiMo_3S_4) using a template-assisted solvothermal method for an alkaline HER. In addition, Kang et al. [39] examined how defect sites influenced the HER/OER activity of hydrothermally prepared NiMo_3S_4 . However, due to fewer catalytic active sites in the bare form of the Chevrel-phase, the NiMo_3S_4 exhibits promising electrocatalytic activity at relatively low current densities ($<100 \text{ mA cm}^{-2}$) and require high overpotentials to reach high current densities ($>100 \text{ mA cm}^{-2}$) [4,41]. Hence, the high current density overall water splitting performance and the fundamental kinetics of reaction intermediates for bifunctional HER and OER remain unexplored for NiMo_3S_4 -based Chevrel-phases.

Usually, the electrocatalytic HER and OER activity of electrocatalysts can be efficiently optimized by basal plane activation, interface engineering, hybrid formation, employing nano-size effects, and electronic modulation [42–48]. Recent experimental and theoretical investigations indicate that the delocalization of local electron distribution around active sites is an effective approach to synergistically optimize the active sites and thereby increase the intrinsic activity and adsorption/desorption properties through a d-electron density modulation strategy [1, 48–50]. Intense research has been made by Vante et al. [32] whereby metal ion-doped Mo_6Se_8 clusters can enhance the electrocatalytic HER and ORR performance by enrichment of the d-state electron density. Chen et al. [50] reported that an ultrathin two-dimensional (2D) nanosheet architecture can effectively delocalize the Ni d-electrons of NiSe_2 , which can strongly influence the OER activity. Wang et al. [1] utilized a delocalization strategy to optimize the HER/OER kinetics of $\text{NiS}_{0.5}\text{Se}_{0.5}$ nanosheets @ $\text{NiS}_{0.5}\text{Se}_{0.5}$ nanorods structures through the coupling of single-atom of tungsten (W- $\text{NiS}_{0.5}\text{Se}_{0.5}$), which resulted in an enhanced electrocatalytic activity by increasing the d-electron density. In addition, Zhang et al. [49] observed that the incorporation of V atoms can lead to an increase in the charge density of a $\text{Co(P)}/\text{Co(O)}$ heterostructure, resulting in a lower kinetic energy barrier and promoting bifunctional HER/OER activity. Hence, optimizing the charge density of active sites through a d-electron delocalization is of significant interest to enhance the electrocatalytic HER and OER performance. Unfortunately, a detailed understanding the underlying science of the intrinsic kinetic mechanism for electrocatalytic HER/OER and appropriate d-electron delocalization strategy for Chevrel-phase ternary metal sulfides remains unexplored.

Therefore, by utilizing a delocalization of d-electron density strategy,

we demonstrate that novel ultrathin nanosheets of Chevrel-phase nickel molybdenum sulfide (NiMo_3S_4) can be formed by a facile hydrothermal method through two different sulfur (S) precursors. Furthermore, to increase the exposed edge active sites and enrich the d-electron density around the edge active Ni atoms, a range of metal dopants and amounts ($\text{M} = \text{Co, Fe, or Cu}$ at $\sim 0.5, 0.75, 1.00$, and 1.25 mL of 0.2 mM L^{-1} of metal dopant precursor solutions) were introduced. Thiourea (TU) was used as an S source to form ultrathin nanosheets of Chevrel-phase $\text{M/N-NiMo}_3\text{S}_4$ ($\text{M} = \text{Co, Fe, and Cu}$) catalysts with optimal amounts of chemical components to create extra edges, while the metal dopants resulted in a high d-electron density around the Ni edge active sites to provide excellent bifunctional HER/OER and overall water splitting performance. For convenience, hereafter, we refer to the electrocatalysts made by the precursors of TU with 1.00 mL Co , 1.00 mL Fe and 1.25 mL Cu precursor as $\text{Co/N-NiMo}_3\text{S}_4$, $\text{Fe/N-NiMo}_3\text{S}_4$, and $\text{Cu/N-NiMo}_3\text{S}_4$ respectively. Due to the increased d-electron density by incorporation of Co at nearby Ni edge active sites and an upshift in the d-band center, the optimized ultrathin nanosheets of $\text{Co/N-NiMo}_3\text{S}_4$ are able to regulate the free energies of various reaction intermediates such as H^* , OH^* , O^* , OOH^* for water adsorption/dissociation. As a result, the $\text{Co/N-NiMo}_3\text{S}_4$ exhibits an excellent HER and OER activity in terms of ultra-low overpotentials of $\sim 78, 208, 282, 307 \text{ mV}$ at $10, 100, 500, 1000 \text{ mA cm}^{-2}$; and $186, 204$, and 225 mV , at $50, 100$, and 300 mA cm^{-2} , respectively, compared to all other samples. The $\text{Co/N-NiMo}_3\text{S}_4$ electrolyzer exploiting the electrocatalyst as both cathode and anode provides outstanding overall water splitting activity, requiring a low cell voltage of $\sim 1.47 \text{ V}$ at 10 mA cm^{-2} .

2. Experimental section

2.1. Materials and methods

All chemical reagents, including sodium molybdate ($\text{Na}_2\text{MoO}_4 \cdot 2\text{H}_2\text{O}$), ammonium molybdate ($(\text{NH}_4)_6\text{Mo}_7\text{O}_{24} \cdot 4\text{H}_2\text{O}$), nickel nitrate ($\text{Ni}(\text{NO}_3)_2 \cdot 6\text{H}_2\text{O}$), iron sulfate ($\text{FeSO}_4 \cdot 7\text{H}_2\text{O}$), cobalt nitrate ($\text{Co}(\text{NO}_3)_2 \cdot 6\text{H}_2\text{O}$), copper sulfate ($\text{CuSO}_4 \cdot 5\text{H}_2\text{O}$), thiourea (TU; $\text{CH}_4\text{N}_2\text{S}$), and sodium sulfide (Na_2S ; anhydrous), were purchased from Sinopharm (Beijing, China), Aladdin (Shanghai, China), and used without any further purification.

2.1.1. Synthesis of MoS_2

In a typical process, 3.5 mM of sodium molybdate and 35 mM Na_2S were dissolved into 80 mL of deionized water and stirred for 1 h . Afterward, 2 mL acetic acid was added and stirred for 30 min . Then, the solution was transferred into a 100 mL PTFE-lined stainless steel autoclave and heated at 180°C for 16 h . The MoS_2 sample was obtained by filtration and washed more than ten times with water and ethanol, in sequence, and then dried at 60°C for 24 h .

2.1.2. Synthesis of N-MoS_2

Initially, 3.5 mM of ammonium molybdate and 35 mM of thiourea were dissolved into 80 mL of deionized water and stirred for 1 h . Then the solution was transferred into a 100 mL PTFE-lined stainless steel autoclave and heated at 180°C for 16 h . The N-MoS_2 sample was obtained by filtration and washed more than ten times with water and ethanol, in sequence, and then dried at 60°C for 24 h .

2.1.3. Synthesis of NiMo_3S_4

At first, 3.5 mM of sodium molybdate, 1.0 mM of nickel nitrate, and 70 mM Na_2S were dissolved into 80 mL of deionized water and stirred for 1 h . Afterward, 2 mL acetic acid was added and stirred for 30 min . Then the solution was transferred into a 100 mL PTFE-lined stainless steel autoclave and heated at 180°C for 16 h . Then the NiMo_3S_4 sample was obtained by filtration and washed more than ten times with water and ethanol, in sequence, and then dried at 60°C for 24 h .

2.1.4. Synthesis of N-NiMo₃S₄

Initially, 3.5 mM of sodium molybdate, 1.0 mM of nickel nitrate, and 70 mM of thiourea were dissolved into 80 mL of deionized water and stirred for 1 h. Then the solution was transferred into a 100 mL PTFE-lined stainless steel autoclave and heated at 180 °C for 16 h. Then the N-NiMo₃S₄ sample was obtained by filtration and washed more than ten times with water and ethanol, in sequence, and then dried at 60 °C for 24 h.

2.1.5. Synthesis of M/N-NiMo₃S₄ (M = Co, Fe, and Cu)

In a typical process, 3.5 mM of sodium molybdate, 1.0 mM of nickel nitrate, and 70 mM of thiourea were dissolved into 80 mL of deionized water and stirred for 1 h. Then, different volumes (*i.e.*, 0.5 mL, 0.75 mL, 1.00 mL, and 1.25 mL) of 0.2 mM L⁻¹ of Co solution prepared using cobalt nitrate in deionized water were then added followed by 30 min of stirring. Finally, the solution was transferred into a 100 mL PTFE-lined stainless steel autoclave and heated at 180 °C for 16 h. Then the Co/N-NiMo₃S₄ samples were obtained by filtration and washed more than ten times with water and ethanol, in sequence, and then dried at 60 °C for 24 h. Similarly, to achieve the Fe/N-NiMo₃S₄ and Cu/N-NiMo₃S₄ samples, different volumes of 0.2 mM L⁻¹ of Fe and Cu precursors were prepared using iron sulfate, and copper sulfate in deionized water was used respectively instead of Co solution.

2.1.6. Synthesis of Co-NiMo₃S₄

The synthesis of Co-NiMo₃S₄ is similar to Co/N-NiMo₃S₄, while the Na₂S was used instead of thiourea.

2.2. Characterizations

The microstructure, surface morphology, and elemental mapping of the prepared samples were examined by scanning electron microscopy (JSM-6380LV) and high-resolution transmission electron microscopy (TEM and STEM, JEOL, JEM-2100F), equipped with an energy-dispersive X-ray spectrometer (EDS). A PANalytical X'Pert³ powder X-ray diffractometer equipped with Cu K α radiation (wavelength = 0.15406 nm) was used to investigate the phase and crystalline nature of the prepared catalysts. The functional groups present in the prepared samples were identified by a Thermo Scientific Nicolet iS10 Fourier transform infrared (FTIR) spectrophotometer. A Renishaw in Via Raman microscope apparatus, attached with an Ar⁺ laser (~514 nm) was used to acquire the Raman spectra. The chemical composition and valance states of the prepared samples were analyzed using Thermo Fisher Scientific K-alpha X-ray Photoelectron Spectrophotometer (XPS). AJW-BK112 Surface Area and Mesopore Size Analyser, JWGB Instrument, China was used to acquire the N₂ adsorption-desorption isotherms. A Bruker A300 Electron Hymagnetic Resonance Spectrometer was used to measure the Electron Spin Resonance (ESR) spectra at room temperature and the Inductively Coupled Plasma-Optically Emitting Spectra (ICP-OES) were measured on PerkinElmer's new Avio™ 200.

2.3. Electrochemical experiments

All electrochemical measurements were carried out on a CHI 660E potentiostat CH Instruments Inc., (Shanghai, China). The working electrode and catalyst ink was prepared according to Wu et al. [46] method, *i.e.*, dispersing the catalyst (5 mg) and Nafion solution (5 wt%, 50 μ L) in ethanol (950 μ L). The dispersion (100 μ L) was drop-cast onto a carbon cloth, with a catalyst loading of ~2.5 mg cm⁻². During the electrochemical measurements, Ag/AgCl (saturated KCl solution) and graphitic rod were used as reference and counter electrodes respectively. An aqueous 1.0 M KOH solution was bubbled with N₂ and O₂ for 30 min before the HER and OER testing respectively. The HER and OER linear sweep voltammograms (LSV) were recorded at a scan rate of 10 mV s⁻¹ with iR compensation (95%), while the background was corrected. To estimate the ECSA of the samples, CV curves were tested to measure the

C_{dl} between 0.15 and 0.25 V vs. RHE for the HER, while 0.8–0.9 V vs. RHE for the OER at different scan rates of 10–100 mV s⁻¹. The EIS was measured at 100 mV for HER, at frequencies ranging from 100 kHz to 1 Hz, and the η of 350 mV for OER. For overall water splitting, the evolved H₂, O₂ gas, and long-term stability for overall water splitting measurements were carried out in a two-electrode H-type air-tight cell separated by a Nafion 115 membrane.

2.4. First-principle calculations

The NiMo₃S₄ is a disordered system, and to provide more precise results, the Supercell program with Special Quasi-random Structures (SQS) approximation was used to construct a primitive (1 \times 1 \times 1) supercell [47]. Further, it has extended to a 2 \times 2 \times 1 supercell in a CASTEP module in Material Studio to perform geometry optimization and spin-polarized electronic calculations. Then (001) facet of NiMo₃S₄ was used as an initial model in CASTEP, Material Studio. Considering the experimental analyses, the prepared samples reveal low-level metal cation substitution to form M/N-NiMo₃S₄ (M = Co, Fe, and Cu), and N (as impurity) is highly preferred in this system. Thus to provide more precise information, one S atom coordinated with an edge Ni atom was exchanged by a Co or Fe or Cu atom, and one S atom has been altered by N to form an M/N-NiMo₃S₄ (M = Co, Fe, and Cu) system to signify the metal coupled system. During electronic structure calculations, a generalized gradient approximation (GGA) of a Perdew-Burke-Ernzerhof (PBE) function was used to describe electron exchange and correlation, while a kinetic energy cut-off of 550 eV was consigned to the plane-wave basis set; ultra-soft pseudopotentials were used. A set of (5 \times 5 \times 1) *k*-mesh was used to optimize the structure and electronic structure until all residual forces declined to below 0.02 eV Å⁻¹. A vacuum level of 15 Å was used along the *z*-direction. For the HER and OER activity calculations, we have used the Quantum Espresso compiled in Winmster V10.6.2, while slab models of (001) were selected with a vacuum thickness of ~15 Å along the *z*-direction. The kinetic energy cut-off of 450 eV and (5 \times 5 \times 1) *k*-mesh was consigned to the plane-wave basis set, the ultra-soft pseudopotentials were used and the self-consistent field (SCF) tolerance was 1 \times 10⁻⁶ eV. Calculations were executed using the spin-polarized PBE exchange-correlation function. In addition, we used the DFT-D3 (BJ) method to consider the van der Waals (vdW) effect in all calculations. The Gibbs free energy of the reaction intermediates such as H, OH, O, and OOH for the HER and OER processes can be calculated by following previous reports; additional details are presented in the [Supporting Information](#) file [45,49].

3. Results and discussion

3.1. Design of bifunctional electrocatalyst

Classically, the Chevrel-phase of NiMo₃S₄ is a disordered structure resulting from the interconnection of a cluster of Mo₆S₈ units (Fig. 1a), where the nickel (Ni²⁺) metal atoms can occupy the edges or free cavities between units that result in the ternary NiMo₃S₄ (Fig. 1b) [31–35]. Based on the collision theory in chemical kinetics, when a cluster of Mo₆S₈ units is surrounded by more Ni²⁺ ions, strong atomic collisions may take place which can result in substitutional and vacancy defects [32]. As a consequence, the continuous growth of the layered structure of NiMo₃S₄ was constrained. Such local atomic structures can exhibit a metallic edge-rich active site nature, which makes the NiMo₃S₄ catalyst a robust material for the HER and OER. In contrast, an inadequate concentration of Ni²⁺ ions may create random defect sites of lower density, which are unable to extensively modify the growth of the layered structures and results in Ni-doped MoS₂ [9]. Meanwhile, the interconnected Mo₆S₈ cluster units allow faster charge transfer kinetics for the HER [30,32,39]. However, a deep understanding of HER and OER electrocatalysis on this Chevrel-phase NiMo₃S₄ is currently lacking. The NiMo₃S₄ phase with an R-3 structure is disordered; while the Ni sites

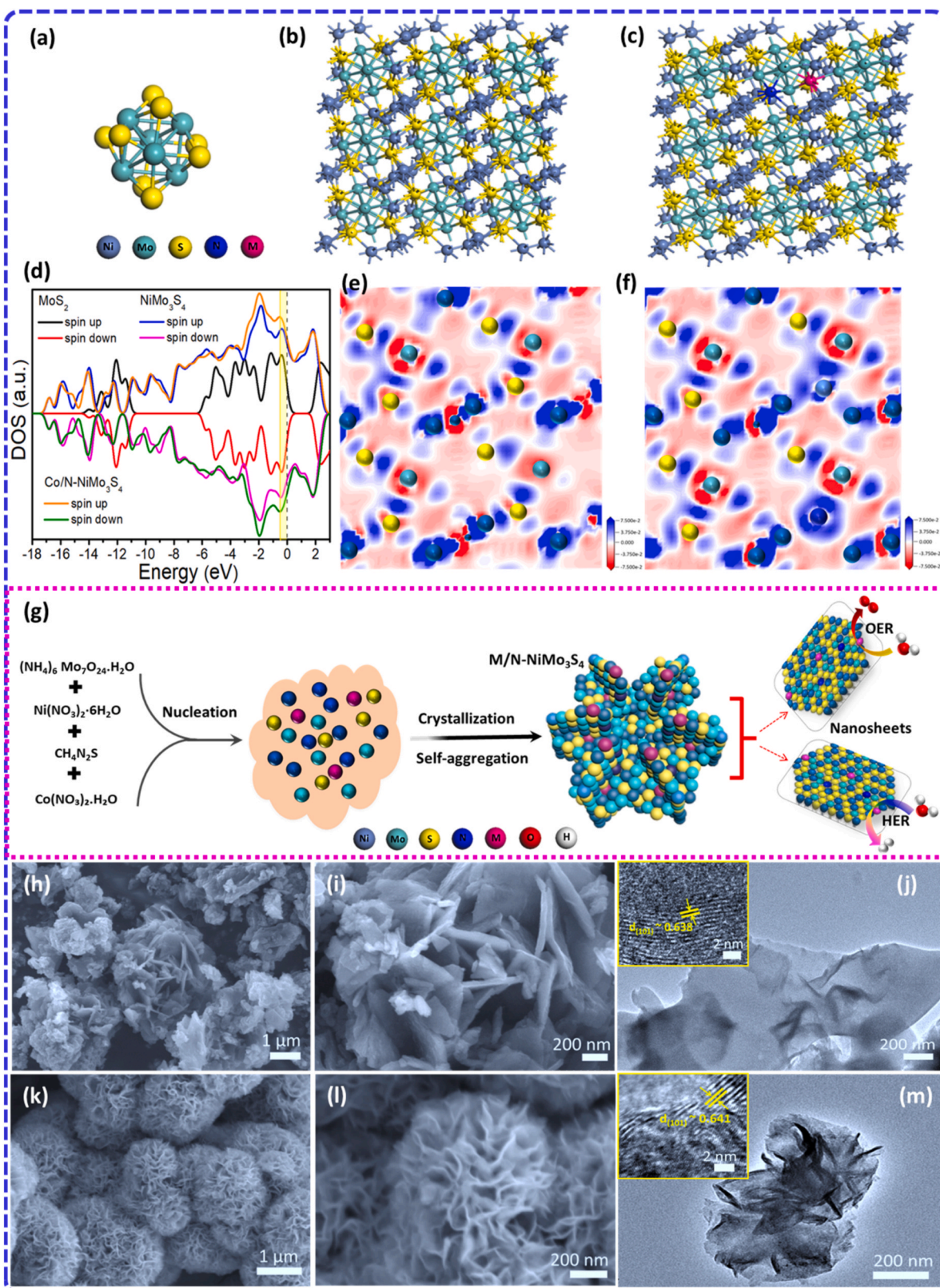


Fig. 1. (a) Mo_6S_8 cluster unit. (b) Crystal structure of active edge sites rich Chevrel-phase NiMo_3S_4 and (c) the proposed d-electron enrichment strategy by coupling metal ions at the nearby Ni edge sites in the Chevrel-phase NiMo_3S_4 (present study) (d) Density of states for the bare MoS_2 , Chevrel-phase NiMo_3S_4 , and $\text{Co/N-NiMo}_3\text{S}_4$. Charge-density difference plots for Chevrel-phase (e) NiMo_3S_4 and (f) $\text{Co/N-NiMo}_3\text{S}_4$. (g) Schematic of synthesis of Chevrel-phase NiMo_3S_4 , $\text{N-NiMo}_3\text{S}_4$, $\text{M/N-NiMo}_3\text{S}_4$ ($\text{M} = \text{Co}, \text{Fe}, \text{and Cu}$) nanosheets via a facile hydrothermal approach. FE-SEM, and TEM images for (h-j) bare NiMo_3S_4 and (k-m) $\text{N-NiMo}_3\text{S}_4$ samples; inserts in (j and m) are the HR-TEM images.

are on the 6 f sites with a 1/6 occupancy; see Fig. 1b, and more additional details are provided in the DFT section. As shown in Fig. 1c, we initially employed theoretical predictions to understand the strategy of d-electron delocalization by incorporating metal atoms ($M = \text{Co}$, Fe , and Cu) in NiMo_3S_4 . When compared to MoS_2 and NiMo_3S_4 , the $\text{Co/N-NiMo}_3\text{S}_4$ phase showed an increased density of states (DOS) for the

unoccupied states from ≈ 0.50 eV to the Fermi level, thereby indicating electron delocalization for the $\text{Co/N-NiMo}_3\text{S}_4$ phase through the coupling of Co atoms with Ni edge atoms (as seen in the shadowed part in Fig. 1d). This results in an increase in the electron density around edge Ni atoms and has been validated by the charge density plots in Fig. 1e-f, which are in good agreement with previous reports [1,49].

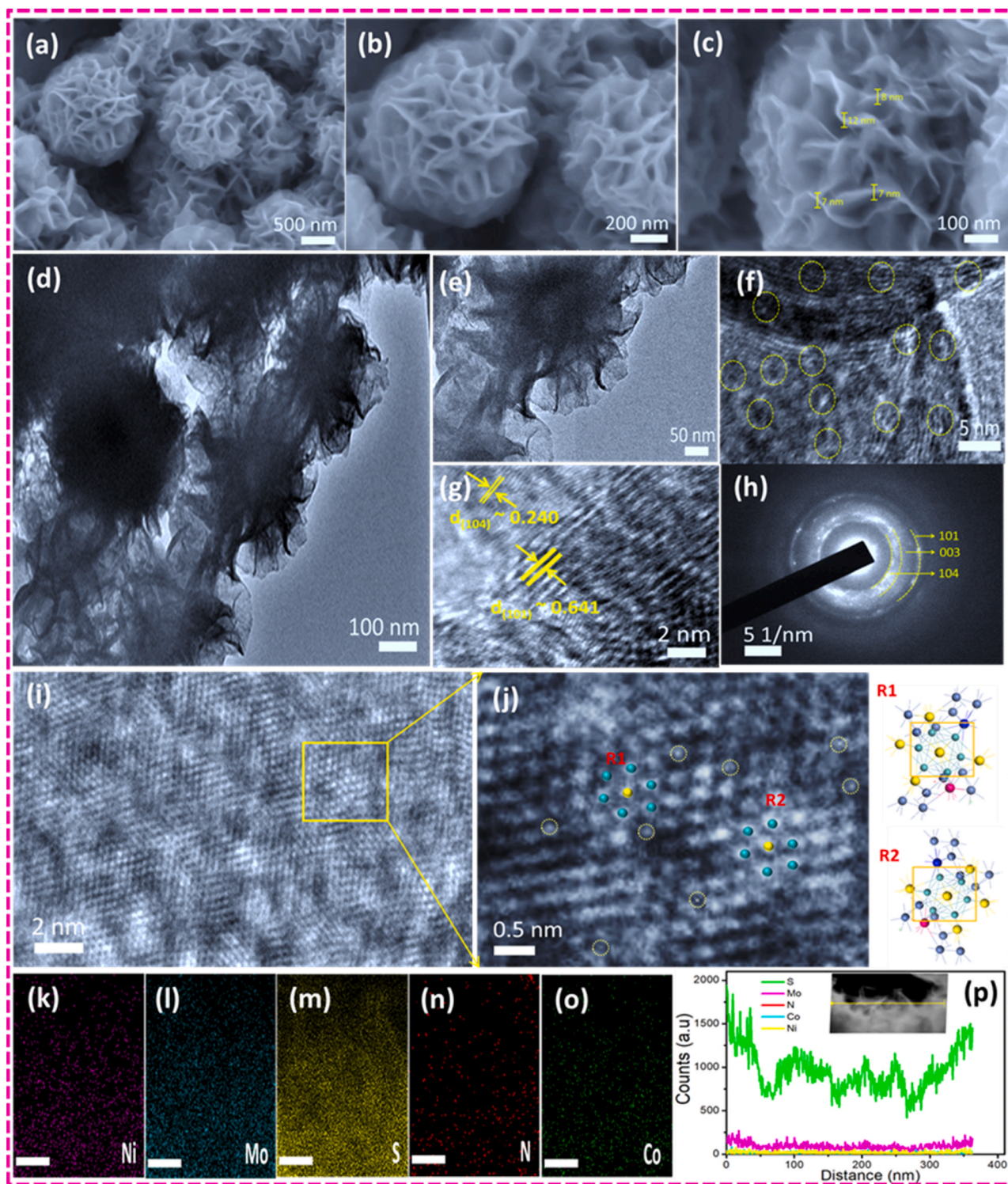


Fig. 2. (a-c) FE-SEM, (d-f) TEM, HR-TEM images (yellow circles highlight the existence of defects) and their corresponding selected area electron diffraction pattern (h) of Chevrel-phase $\text{Co/N-NiMo}_3\text{S}_4$ (i-j) STEM images magnifying the highlighted regions (R1: Region 1 and R2: Region 2) and the $\text{Co/N-NiMo}_3\text{S}_4$ lattice diagram, yellow circles in (j) highlighting the possible location of dopants based on lattice diagram, (k-o) EDS selected area mapping and (p) line spectra of $\text{Co/N-NiMo}_3\text{S}_4$ catalyst.

These results signify that the d-electron density of NiMo_3S_4 can be increased by coupling with metallic Co atoms, and this phenomenon is a highly promising approach for realizing robust bifunctional HER and OER catalysts.

3.2. Characterization of chevrel-phase electrocatalysts

Based on the above discussion, the precise control of the NiMo_3S_4 Chevrel-phase catalyst size and optimization of active electronic sites via metal cation insertion ($M = \text{Co}, \text{Fe}, \text{and Cu}$) during hydrothermal synthesis is achieved using two different precursors as a sulfur (S) source

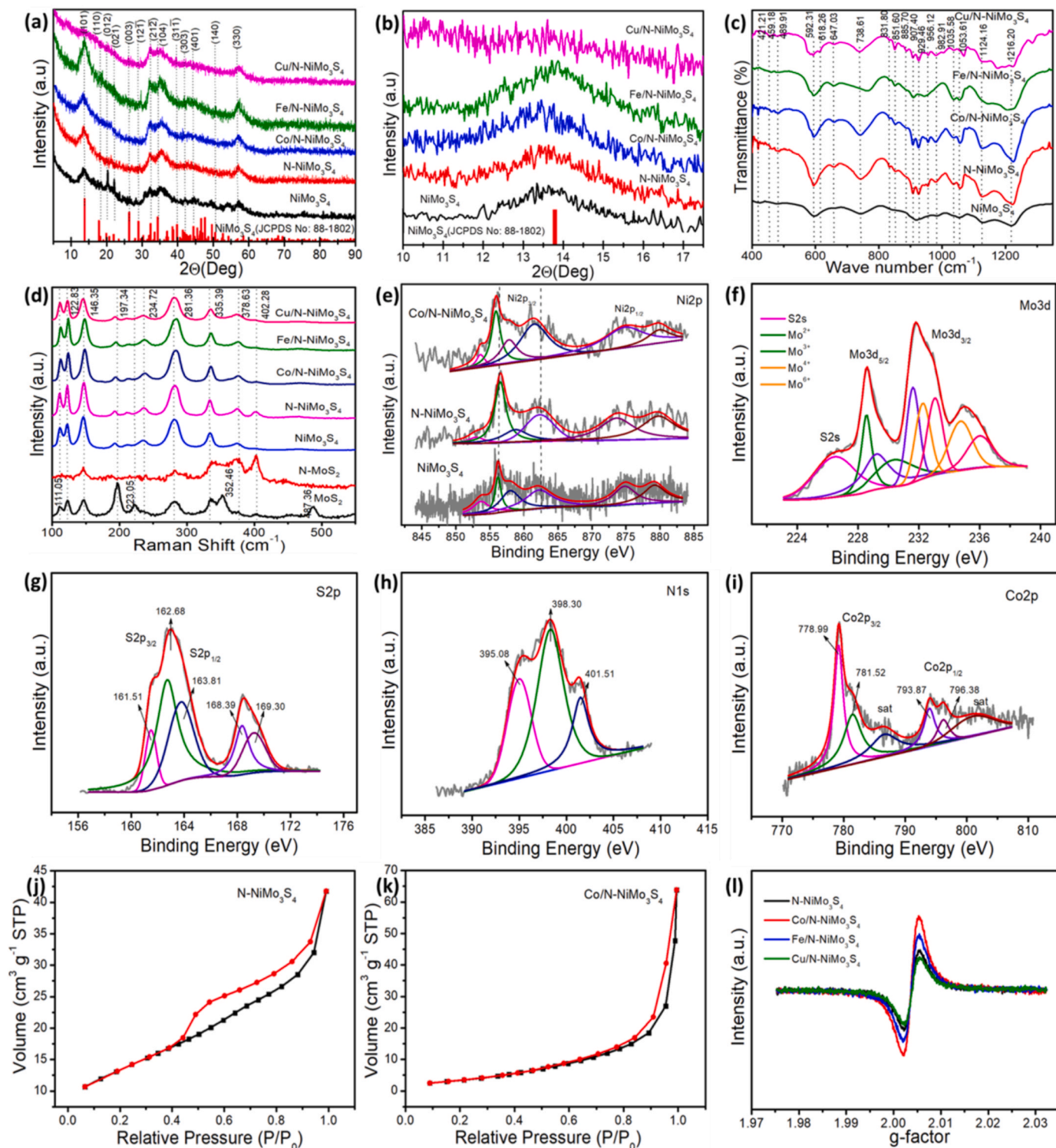


Fig. 3. (a) XRD patterns of prepared Chevrel-phase NiMo_3S_4 , $\text{N-NiMo}_3\text{S}_4$, $\text{Co/N-NiMo}_3\text{S}_4$, $\text{Fe/N-NiMo}_3\text{S}_4$, $\text{Cu/N-NiMo}_3\text{S}_4$ catalysts and their magnified area with the 2θ angles ranging from 10° to 17.5° . (b) (c-d) FT-IR and Raman spectra of prepared Chevrel-phase catalysts. (e) XPS $\text{Ni}2p$ core-level spectra for NiMo_3S_4 , $\text{N-NiMo}_3\text{S}_4$, and $\text{Co/N-NiMo}_3\text{S}_4$. (f-i) XPS spectra for $\text{Mo}3d$, $\text{S}2p$, $\text{N}1s$, and $\text{Co}2p$ core-levels of $\text{Co/N-NiMo}_3\text{S}_4$ catalyst. (j-k) N_2 adsorption and desorption isotherms for $\text{N-NiMo}_3\text{S}_4$ and $\text{Co/N-NiMo}_3\text{S}_4$. (l) ESR spectra of prepared Chevrel-phase $\text{N-NiMo}_3\text{S}_4$, $\text{Co/N-NiMo}_3\text{S}_4$, $\text{Fe/N-NiMo}_3\text{S}_4$, and $\text{Cu/N-NiMo}_3\text{S}_4$ catalysts.

namely; sodium sulfide (Na_2S) and thiourea (TU); see Fig. 1g. As shown in Figs. S1-S2 and Fig. 1(h-j), the bare MoS_2 and NiMo_3S_4 that were fabricated by Na_2S result in the formation of a nanoflake-like morphology. Conversely, when thiourea was used as a S source, all samples contained interconnected ultrathin nanosheets, with an average thickness of $\sim 7\text{--}12\text{ nm}$; see Figs. S3-S4 and Fig. 1(k-m). The interconnected ultrathin nanosheets could be formed due to the by-products of thiourea. During the hydrothermal process for NiMo_3S_4 fabrication, when TU was used as a precursor it could potentially be decomposed into ammonia (NH_3 gas), where the NH_3 gas could diffuse into the S vacancies to form N- NiMo_3S_4 [51–53]. As a result of NH_3 intercalation, nitrogen (N) impurities could attach to the host lattice, at either substitutional and/or interstitial sites, in the as-prepared catalysts thereby resulting in the formation of N- MoS_2 , and N- NiMo_3S_4 catalysts, which was identified by the line and selected area EDS mapping in Figs. S3-S4. Previously, Liu et al., [53] prepared a similar form of N- MoS_2 material on a large scale. The TU could not only act as a source for S, but it could also act as a structural directing agent, and an excess amount of N could dope on the host lattice through NH_3 intercalation (based on the amount of TU precursor content and the reaction conditions). Thus, it is worth noting that, the optimum amount of Ni and Mo precursor ratio with TU will lead to the formation of an ultrathin N- NiMo_3S_4 structure, while the N could be the impurity center. Fig. 2 and Figs. S5-S6 shows microscopic images of metal (M = Co, Fe, and Cu) incorporated with the NiMo_3S_4 catalysts. Compared to the bare MoS_2 and NiMo_3S_4 , the ultrathin nanosheets geometry and random defects formed in N- MoS_2 , N- NiMo_3S_4 , and M/N- NiMo_3S_4 (M = Co, Fe, and Cu) can lead to significant geometric distortion of the basal plane due to the change in bond length and presence of vacancies [9]. In specific, the SEM and TEM images of Co/N- NiMo_3S_4 signify the formation of interconnected ultrathin nanosheets (Fig. 2a-e). The increase in molecular complexity, along with the distortions across the entire basal plane, may further weaken the interaction between the adjacent NiMo_3S_4 layers, thus leading to an enlargement of the interlayer spacing (Fig. 2f-h). In addition, the selected area electron diffraction (SAED) patterns confirm the formation of Chevrel-phase Co/N- NiMo_3S_4 . Remarkably, as shown in Fig. 2i, the HR-TEM image and the magnified regions marked in Fig. 2j resemble the crystal lattice of Co/N- NiMo_3S_4 . Fig. S7 and Fig. 2(k-p) shows the energy-dispersive X-ray spectrum (EDS), which signify the purity and the presence of chemical components in the prepared catalysts.

The crystal structures of prepared samples were examined by X-ray diffraction (XRD) analysis. As shown in Fig. S8, the bare MoS_2 and N- MoS_2 correspond to the crystal structure of cubic phase MoS_2 (JCPDS Card No: 75–1539). Conversely, the bare NiMo_3S_4 prepared by sodium sulfide (Na_2S) exhibits sharp and high-intensity peaks (Fig. 3a). However, when a thiourea precursor was used, weak and broad diffraction peaks were observed for the N- NiMo_3S_4 and M/N- NiMo_3S_4 (M = Co, Fe, and Cu) catalysts, highlighting its low crystalline nature. The XRD pattern of NiMo_3S_4 , N- NiMo_3S_4 , and the M/N- NiMo_3S_4 (M = Co, Fe, and Cu) catalysts is consistent with a standard hexagonal Chevrel-phase NiMo_3S_4 (JCPDS Card No: 88–1802). The broad diffraction peaks indicate the ultrathin flakes are at nanoscale dimensions and the presence of abundant defect sites on N- MoS_2 , N- NiMo_3S_4 M/N- NiMo_3S_4 (M = Co, Fe, and Cu). The magnified area of the XRD pattern with 2θ angles ranging from 10° to 17.5° , where the maximum intensity peak is at 13.7° , confirms the effective formation of a hexagonal NiMo_3S_4 Chevrel-phase; see Fig. 3b. The small shift in the 13.7° peaks for M/N- NiMo_3S_4 (M = Co, Fe, and Cu) signifying a metal atom coupling effect and ultrathin nanosheets features. The absence of other high-angle peaks indicates the disordered structural feature of prepared samples due to the existence of defect sites, which could be produced by local structural deformation by doping and associated lattice strains, which is often observed in several layered compounds [9,39].

Fig. 3c shows the Fourier-Transform Infra-Red (FT-IR) spectra of the prepared samples. Typically, for transition metal sulfide systems, the peaks at low frequencies are caused by sulfidation vibrations. Two bands

located at ~ 421.12 and 489.91 cm^{-1} are related to the inorganic thio-core [9,54]. The bands at ~ 592.31 and 618.26 cm^{-1} could be attributed to the Mo-S and Ni-S stretching vibrational mode [53,54]. For the N- MoS_2 , N- NiMo_3S_4 , and M/N- NiMo_3S_4 (M = Co, Fe, and Cu) the peaks are wider with small shifts, signifying the alteration of bond strength, while the bands at ~ 738.61 , 647.03 , and 831.80 , 851.60 and 885.70 cm^{-1} belong to the S-Mo-S stretching modes [9,54]. The peaks at ~ 907.40 and 929.46 cm^{-1} are due to the S-S stretching modes. The metal sulfur bonds present in the compound are evident from the minor peak at 475 cm^{-1} and may be due to antisymmetric S-M-S stretching. In addition, minor bands at ~ 459.18 , 956.12 , and 982.91 cm^{-1} can be assigned to M-N symmetric and asymmetric stretching vibrations [53]. The peaks around $1000\text{--}1100$ and $1050\text{--}1110\text{ cm}^{-1}$ could be attributed to sulfoxide- and nitrito-complexes respectively [47]. The peak at 1124 cm^{-1} is attributed to the NH_2 rocking mode and is not affected by the coordination.

As shown in Fig. 3d, the Raman peaks are attributed to the formation of highly distorted metallic structures. The peaks at ~ 111.05 , 122.83 , 146.35 , 335.39 , 352.46 , 378.63 , 402.28 , and 487.36 cm^{-1} were accredited to the in-plane vibrations of Eg modes. The peaks at ~ 197.34 , 223.05 , 234.72 , and 281.36 cm^{-1} were attributed to the out-plane vibrations of the A1g modes. These results are consistent with previous reports on MoS_2 , N- MoS_2 , and Chevrel-phases [9,46,55]. Significantly, when compared to N- MoS_2 and N- NiMo_3S_4 , the metal (M = Co, Fe, and Cu) incorporated M/N- NiMo_3S_4 spectra show peaks consistent with bare samples, however small shifts, and an intensity increase in frequency, and as well new peaks were being observed for M/N- NiMo_3S_4 Chevrel-phases. The broadening of A1g peaks in N- NiMo_3S_4 and metal (M = Co, Fe, and Cu) doped M/N- NiMo_3S_4 could be ascribed to reduced numbers of stacked layers [9,54]. The shifts in existing modes and new peaks can result from several factors, such as the mass difference of dopants (M), N, and Ni compared to Mo and/or S, a change in bond strengths and also breaking of the symmetries by induced strain or doping. However, the increased intensities of the Raman spectra may be due to in-gap states due to metal (M = Co, Fe, and Cu) and Ni-substitution, signifying the metallic nature of the prepared Chevrel-phases of NiMo_3S_4 , N- NiMo_3S_4 , and M/N- NiMo_3S_4 . The reduced peak intensities at ~ 197.34 , 223.05 , 402.28 , and 487.36 cm^{-1} reveal the existence of in-plane defect sites in the M/N- NiMo_3S_4 samples [9,46,54,55]. Hence, the dissimilar behaviour observed in the IR/Raman spectroscopy may be due to in-plane crystallite size, the effects of several layers, the concentration of Ni, and the effects of metal dopants [9,54]. These results suggest the highly distorted nature of the M/N- NiMo_3S_4 samples, which is consistent with XRD and microscopy observations (Fig. 2 and Fig. 3a). The chemical composition and surface electronic states of prepared catalysts were further explored by X-ray photoelectron spectroscopy (XPS); see Figs. S9-S14 and Fig. 3(e-i). As shown in Figs. S9-S10, the core-level XPS spectra show the existence of Mo, S for pristine MoS_2 and N, Mo, and S for N- MoS_2 . The XPS spectra of Ni 2p for NiMo_3S_4 , N- NiMo_3S_4 , and M/N- NiMo_3S_4 (M = Co, Fe, and Cu) are shown in Fig. 3e, and Figs. S13-S14 and these fit well with the spin-orbit doublet of Ni, and these are close to the previous reports of NiMo_3S_4 and Ni-Mo-S [9,39,45]. Notably, the high-intensity Ni 2p peaks of Co/N- NiMo_3S_4 (855.72 , 861.38 , 874.19 eV), Fe/N- NiMo_3S_4 (855.89 , 861.62 , 874.36 eV) and Cu/N- NiMo_3S_4 (855.76 , 861.39 , 874.18 eV) displayed a slight negative shift as compared to those of NiMo_3S_4 (856.18 , 862.08 , 874.81 eV), N- NiMo_3S_4 (856.51 , 861.68 , 874.23 eV). This designates the effect of electronic coupling of Ni with the metal dopants. However, it is also suggested that, compared to other metal cations, due to the high negative shifts, the use of Co could be more suitable to improve electrocatalytic performance through d-electron density enrichment of the Co/N- NiMo_3S_4 phase (Fig. 3e) [50,56]. In addition, the peaks located at 853.46 and 874.19 eV can be assigned to Ni^{2+} , and the peaks at 855.72 and 879.51 eV indicate the existence of Ni^{3+} in the Co/N- NiMo_3S_4 sample. Likewise, it signifies that both divalent and trivalent Ni elements can exist in all samples [57]. As

shown in Fig. 3f and Fig. S11–S14, the Mo3d spectra of all samples overlapped with the S2s transition, and it can be deconvoluted into eight peaks. As shown in Fig. S11, the Mo3d of NiMo₃S₄ signify the oxidation state could be approximately + 6, while the oxidation state of S can be assigned to − 2 (i.e., 161.21 eV). Hence, ~ 20 electrons (e[−]) remain in the intra-cluster Mo₆X₈ units which can provide a pool of charges that can be involved in an electrocatalytic reaction with a minimum electronic loss or relaxation [30]. In addition, the electronic states of N-NiMo₃S₄ and M/N-NiMo₃S₄ were highly modified, while the + 6 oxidation peak is more visible for Mo3d; see Fig. 3f and Figs. S12–S14. These results indicate that dopants and an ultrathin nature can also modulate the electronic structure of the Chevrel-phase. The Mo3d5/2 peak at 228.3 eV is a good fit with the values reported for layer-type transition metal chalcogenides, where the Mo³⁺ species is presumably related to the formation of Mo–N through the intercalation of NH₃ from thiourea [53].

Previously, Vante et al.[58] proposed that doping could lead to a change in the Mo₆X₈ cluster geometry due to the size of the atoms and band-filling effects, while an optimal level of doping can increase the electronic density near the Fermi level, which can influence the electrocatalytic performance. In addition, Kobayashi et al.,[59] anticipated that doping of Sn can modulate the electronic nature of the Chevrel-phase. The S2p spectra exhibit peaks at 162.68 and 168.41 eV, which could be attributed to S–Metal atoms (Fig. 3g) [30]. Whereas, the deconvoluted peak at 161.51 eV corresponds to the Co atom doped bi-metal sulfide feature [60,61]. The appearance of a shoulder peak at higher binding energies in the S2p region can serve as further evidence for the presence of Mo with higher oxidation states [30]. The N1s peak could be due to NH₃ intercalation see Fig. 3h. As shown in Fig. 3i, the XPS spectrum of Co 2p shows the broad peaks centered at 779.09 and 795.64 eV are associated with Co 2p_{3/2} and Co 2p_{1/2}, respectively. Notably, the deconvoluted high-intensity peak at 778.99 eV is attributed to Co⁺ metal ion, this signifies the doping effect with Ni atoms, which is in good agreement with the XRD (Fig. 3a–b), and previous results (i.e., formation of Co–Ni structure)[62]. The low-intensity peaks positioned at 781.52 and 796.38 eV can be credited to Co²⁺ and Co³⁺ respectively. The intensity of the peaks indicates that Co⁺ metal ion is the dominant state of Co and may be formed Co–Ni bond near the edge surface of the Co/N-NiMo₃S₄ Chevrel-phase catalyst, it could apparently induce d-electrons enrichment at edges (Fig. 3e). Further, the chemical compositions were estimated from XPS, EDS and ICP/OES measurements; as outlined in Table S1. Due to its porous ultrathin nature, the Co/N-NiMo₃S₄ Chevrel-phase catalyst exhibits a higher surface area (59.91 m² g^{−1}) than Fe/N-NiMo₃S₄ (31.82 m² g^{−1}), Cu/N-NiMo₃S₄ (24.96 m² g^{−1}) and N-NiMo₃S₄ (29.93 m² g^{−1}); see Fig. 3j–k and Fig. S15. Furthermore, Electron Spin Resonance (ESR) measurements were carried out to reveal the accumulation of unpaired electrons in the prepared Chevrel-phase catalysts; see Fig. 3l. Remarkably, the Co/N-NiMo₃S₄ exhibits a higher ESR signal than the Fe/N-NiMo₃S₄, Cu/N-NiMo₃S₄ and N-NiMo₃S₄ phases. Considerably, this enhancement could be related to the increased number of unpaired electrons after metal doping, which can have a significant role in the enrichment for the d-electron density of Co/N-NiMo₃S₄, compared to the other prepared catalysts [63–65]. Therefore, the formation of a porous nature with highly exposed edge active sites in the ultrathin Co/N-NiMo₃S₄ Chevrel-phase, and its enrichment of d-electrons suggests that it is likely to provide increased alkaline bifunctional HER/OER kinetics.

3.3. Electrocatalytic activity evaluation

3.3.1. Electrocatalytic HER performance

The electrocatalytic activity of the M/N-NiMo₃S₄ (M = Co, Fe, and Cu) was estimated by linear sweep voltammetry (LSV) on a carbon cloth in an N₂-saturated 1.0 M KOH electrolyte, where bare MoS₂, N-MoS₂, NiMo₃S₄, N-NiMo₃S₄, and Pt/C were used as references. Polarization curves measured at a scan rate of 10 mV s^{−1} are shown in Fig. 4a. The

Co/N-NiMo₃S₄ exhibits a very low HER overpotential of 78, 208, 282, and 307 mV at current densities of 10, 100, 500, and 1000 mA cm^{−2}, respectively, which is noticeably outperforming Fe/N-NiMo₃S₄ (98, 239, 326, 356 mV), Cu/N-NiMo₃S₄ (108, 277, 383, 410 mV), N-NiMo₃S₄ (144, 308, >456 mV), NiMo₃S₄ (161, 353, >485 mV), N-MoS₂ (179, >567 mV), bare MoS₂ (239, >624 mV), and Pt/C (29, >162 mV). Significantly, Fig. 4b, which is an enlarged view of the low overpotential region in Fig. 4a, shows that the electrocatalytic HER performance of Co/N-NiMo₃S₄ outperforms the benchmark of Pt/C at a current density of 200 mA cm^{−2} (Fig. 4b). The superior HER activity of ultrathin Co/N-NiMo₃S₄ electrocatalyst is also evidenced by a small Tafel slope of 69 mV dec^{−1}, which outperforms the bare MoS₂ (188 mV dec^{−1}), N-MoS₂ (163 mV dec^{−1}), NiMo₃S₄ (114 mV dec^{−1}), N-NiMo₃S₄ (108 mV dec^{−1}), Fe/N-NiMo₃S₄ (83 mV dec^{−1}) and Cu/N-NiMo₃S₄ (88 mV dec^{−1}) indicating the superior intrinsic HER activity of Co/N-NiMo₃S₄ (Fig. 4c). The HER performance of M/N-NiMo₃S₄ (M = Co, Fe, and Cu) prepared with different amounts of metal precursors is shown in Fig. S16. The highest C_{dl} values for the Co/N-NiMo₃S₄ for all the catalysts imply an enriched electrochemically active surface area (ECSA) and the low R_{ct} value suggests rapid charge transfer and improved charge transfer of Co/N-NiMo₃S₄. Both the NiMo₃S₄ and N-NiMo₃S₄ showed more modest HER performance as a result of inadequate active sites, lower ECSA, and large dead volume; nevertheless, they are higher than MoS₂ and N-MoS₂ (Figs. S17–S18). Moreover, the ECSA normalized and mass normalized results of Co/N-NiMo₃S₄, Fe/N-NiMo₃S₄, Cu/N-NiMo₃S₄, N-NiMo₃S₄, and NiMo₃S₄ indicate the enriched activity of Co/N-NiMo₃S₄ for the HER; see Fig. S19. As a result, the Co/N-NiMo₃S₄ exhibits an excellent mass activity of 400 mA mg^{−1} at an overpotential of 305 mV, which is.

superior to other electrocatalysts. To realize the intrinsic electrocatalytic activity of each active site, the turnover frequency (TOF) was considered. The turnover frequency of the HER electrocatalysts at an overpotential of 200 mV vs. RHE is in the order of Co/N-NiMo₃S₄ (21.2 s^{−1}) > Fe/N-NiMo₃S₄ (12.99 s^{−1}) > Cu/N-NiMo₃S₄ (6.29 s^{−1}) > N-NiMo₃S₄ (3.99 s^{−1}) > NiMo₃S₄ (3.21 s^{−1}) respectively (Figs. S20–S21). This signifies that in a Co/N-NiMo₃S₄ electrocatalyst, the Ni edge sites can ease water dissociation with high turnover frequencies, whereas the doping of Co sites can make it moderate for H₂ gas evolution and release[16]. The HER result signifies that the high intrinsic activity of Co/N-NiMo₃S₄ could be due to the addition of Co atoms. Durability is known to be a pivotal criterion for the practical application of catalysts, as a consequence, the time-dependent current density curves confirm that there is a negligible change in the current densities of 100 and 500 mA cm^{−2} at 208 and 282 mV vs. RHE when tested for over 24 h; see Fig. 4d.

Fig. 4e shows a detailed description of the electrocatalytic alkaline HER activity of NiMo₃S₄ and M/N-NiMo₃S₄ (M = Co, Fe, and Cu). During the HER process, the water molecule enters the inner Helmholtz layer that formed at the surface of NiMo₃S₄, N-NiMo₃S₄, and M/N-NiMo₃S₄ [43,66]. In the NiMo₃S₄ or N-NiMo₃S₄ Chevrel-phases, the bond of H–OH in H₂O will be weakened by an interaction between the under-coordinated M^{δ+} metal center (i.e., edge Ni as metal center) and O atom, and the interaction between the dangling S or N atom and H atom (Step 1). In Step 2, the H₂O molecule dissociates into OH[−] and H with the assistance of a free electron. Next, the OH[−] will be adsorbed by M^{δ+} (i.e., edge Ni metal center), whereas the H atom transfers onto a nearby vacant M^{δ+} (i.e., another nearby edge Ni metal active site) to form H_{ads}. Finally, the OH and H_{ads} will be desorbed from active M^{δ+} metal center sites.

Conversely, in a metal-doped system i.e., M/N-NiMo₃S₄, the H–OH bond in H₂O will be weakened by the interaction between the under-coordinated M^{δ+} metal center (i.e., edge Ni as metal center) and O atom as well as the interaction between the doped metal center (M^{δ+}, M = Co, Fe, and Cu) and H atom (Step 1). Then, the H₂O molecule will be dissociated, while the edge metal center of the Ni atom absorbs the OH, and the H atom transfers onto the nearby doped metal center (M^{δ+}, M =

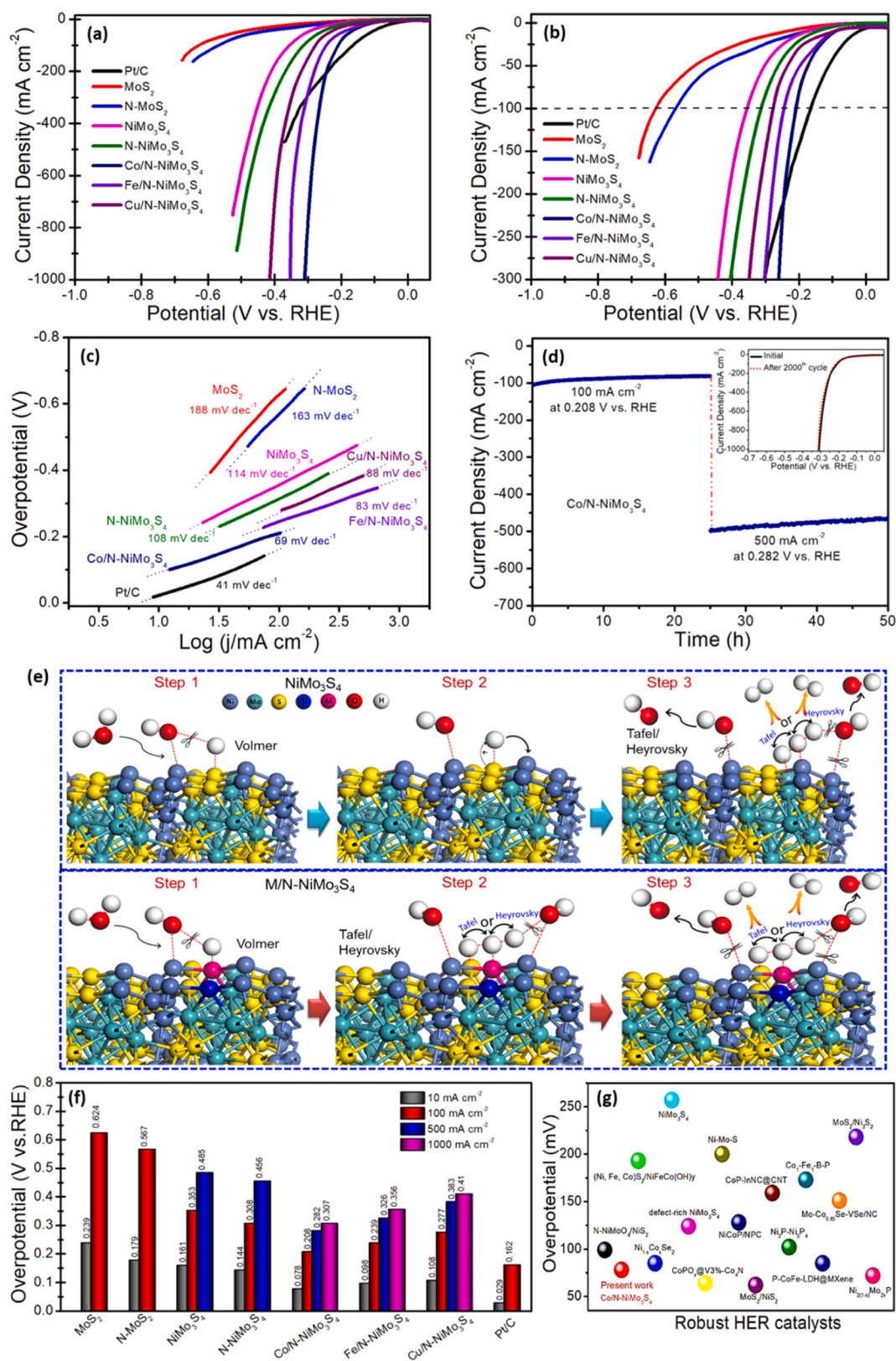


Fig. 4. (a) HER polarization curves of Co/N-NiMo₃S₄, Fe/N-NiMo₃S₄, Cu/N-NiMo₃S₄, N-NiMo₃S₄, NiMo₃S₄, N-MoS₂, MoS₂, and Pt/C in N₂-saturated 1.0 M KOH. (b) Enlarged view of the low overpotential region in (a). (c) Corresponding Tafel plots acquired from (a). (d) Chronoamperometry curves of Co/N-NiMo₃S₄ at a current density of 100 mA cm⁻² at 0.208 V and 500 mA cm⁻² at 0.282 V vs. RHE. Inset: polarization curves of Co/N-NiMo₃S₄ for the HER stability test before and after 2000 CV cycles. (e) Schematic of proposed water dissociation mechanism for NiMo₃S₄, M/N-NiMo₃S₄ (M = Co, Fe, and Cu) in alkaline solutions with atomic models. (f) HER performance and their low overpotentials of Co/N-NiMo₃S₄, Fe/N-NiMo₃S₄, Cu/N-NiMo₃S₄, N-NiMo₃S₄, NiMo₃S₄, N-MoS₂, MoS₂, and Pt/C prepared in the present study. (g) Comparison of HER low overpotentials value of Co/N-NiMo₃S₄ with previously reported robust HER electrocatalysts.

Co, Fe, and Cu) site to form H_{ads} (Step 2). Finally, the adsorbed OH and H_{ads} will be desorbed from active metal center sites. Notably, the adsorption/desorption behavior of OH and H_{ads} intermediates mainly depends on the electronic structure of the catalyst, which governs the thermodynamics and kinetics of water dissociation [43,44,66]. Therefore, the enhanced d-electrons around edge Ni atoms due to the coupling of metal atoms in the M/N-NiMo₃S₄ system could be the reason for the enhanced activity compared to NiMo₃S₄ and N-NiMo₃S₄; additional details will be discussed in the section on first principle calculations. It has been widely validated that, in an alkaline environment, the Co atom is more highly active for the Heyrovsky and Tafel steps than the Ni atom

[45,66]. As a result, the Co/N-NiMo₃S₄ shows the highest intrinsic catalytic activity compared to all other catalysts and outperforms most of the reported non-precious HER electrocatalysts (Fig. 4f-g and Table S2) [9,26,30,42].

3.3.2. Electrocatalytic OER performance

As shown in Fig. 5a, the electrocatalytic OER performance of M/N-NiMo₃S₄ (M = Co, Fe, and Cu) was assessed by LSV, and those of bare MoS₂, N-MoS₂, NiMo₃S₄, N-NiMo₃S₄, and RuO₂ was used as a reference. In comparison with bare MoS₂ (990, >1052 mV), N-MoS₂ (935, >1015 mV), NiMo₃S₄ (401, 459, 755 mV), N-NiMo₃S₄ (370, 400,

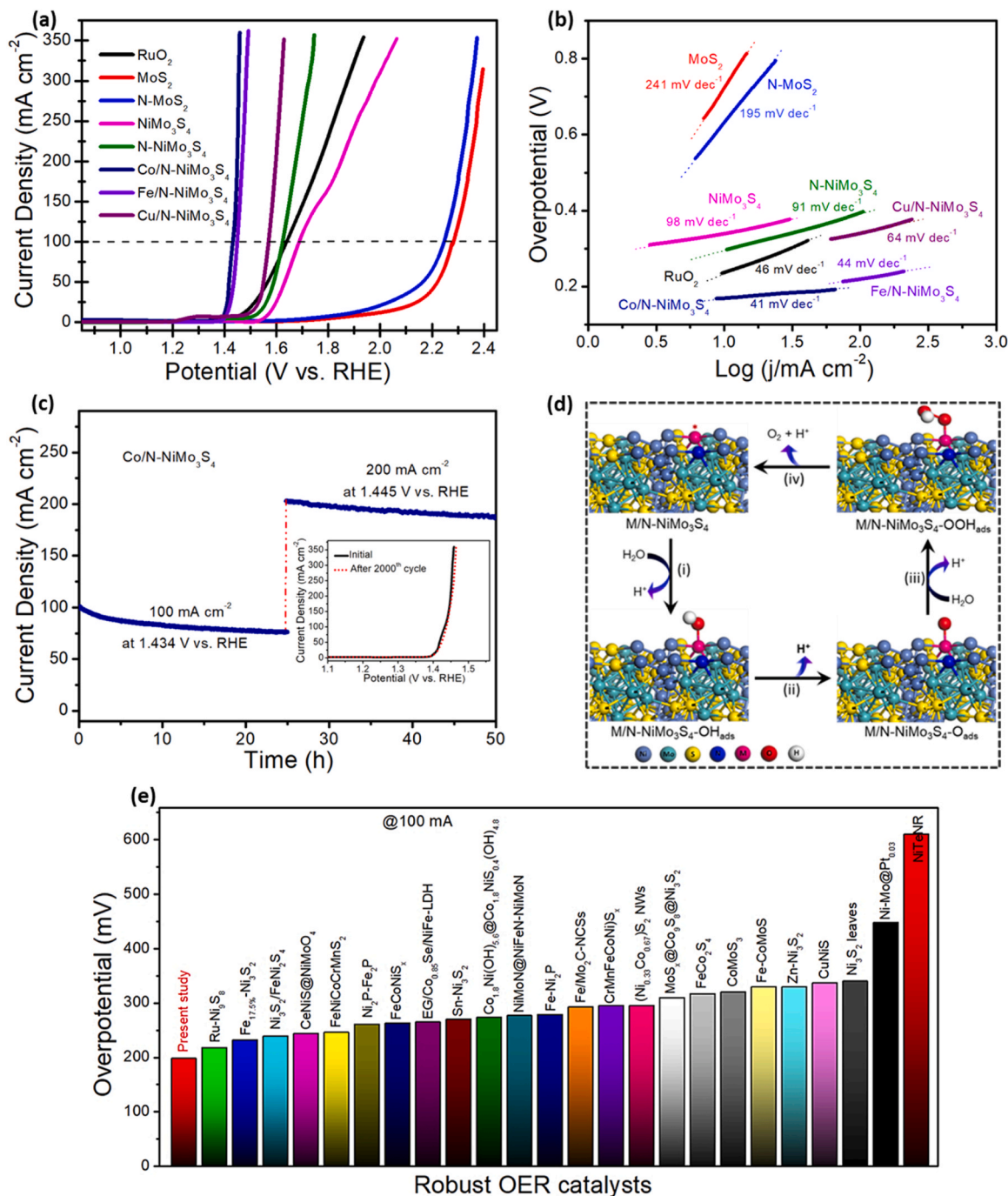


Fig. 5. (a) OER polarization curves of Co/N-NiMo₃S₄, Fe/N-NiMo₃S₄, Cu/N-NiMo₃S₄, N-NiMo₃S₄, NiMo₃S₄, N-MoS₂, MoS₂, and RuO₂ in O₂-saturated 1.0 M KOH. (b) Corresponding Tafel plots acquired from (a). (c) Chronoamperometry curves of Co/N-NiMo₃S₄ at a current density of 100 mA and 200 mA cm^{-2} . Inset: polarization curves of Co/N-NiMo₃S₄ for the OER stability test. (d) Schematic of proposed OER mechanism for M/N-NiMo₃S₄ (M = Co, Fe, and Cu) with atomic models. (e) Comparison of OER low overpotentials value of Co/N-NiMo₃S₄ with previously reported robust OER electrocatalysts.

499 mV), Fe/N-NiMo₃S₄ (211, 225, 246 mV), Cu/N-NiMo₃S₄ (319, 350, 390 mV) and RuO₂ (338, 402, 650 mV), the Co/N-NiMo₃S₄ displays an excellent OER activity with ultralow overpotentials (η) of 186, 204, and 225 mV, at 50, 100, and 300 mA cm⁻², respectively. The excellent OER activity of ultrathin Co/N-NiMo₃S₄ electrocatalyst is also revealed by the small Tafel slope of 41 mV dec⁻¹ and it outperforms the bare MoS₂ (241 mV dec⁻¹), N-MoS₂ (195 mV dec⁻¹), NiMo₃S₄ (98 mV dec⁻¹), N-NiMo₃S₄ (91 mV dec⁻¹), Fe/N-NiMo₃S₄ (44 mV dec⁻¹) Cu/N-NiMo₃S₄ (64 mV dec⁻¹) and RuO₂ (46 mV dec⁻¹) indicating the superior intrinsic activity of Co/N-NiMo₃S₄ (Fig. 5b). The performance of M/N-NiMo₃S₄ (M = Co, Fe, and Cu) prepared for different amounts of metal precursors are shown in Fig. S22. Furthermore, to evaluate the specific activities of M/N-NiMo₃S₄ (M = Co, Fe, and Cu), N-NiMo₃S₄, and NiMo₃S₄, electrochemical surface areas (ECSAs) were estimated from the double-layer capacitance (C_{dl}), see Fig. S23. The C_{dl} of Co/N-NiMo₃S₄ (102.3 mF cm⁻²) is much greater than that of NiMo₃S₄ (20.3 mF cm⁻²) and N-

NiMo₃S₄ (23.6 mF cm⁻²). To evaluate the intrinsic activity, the ECSA normalized and mass normalized results of Co/N-NiMo₃S₄, Fe/N-NiMo₃S₄, Cu/N-NiMo₃S₄, N-NiMo₃S₄, and NiMo₃S₄ specify the high activity of Co/N-NiMo₃S₄ for the OER (Fig. S24). The electrochemical impedance spectra (EIS) collected at η = 350 mV show the small charge-transfer resistance (R_{ct}) of Co/N-NiMo₃S₄, suggesting a faster charge transfer kinetics for Co/N-NiMo₃S₄ compared to bare samples (Fig. S25). In addition, the Co/N-NiMo₃S₄ can sustain the OER performance at 100 and 200 mA cm⁻² with the potentials of 1.434 and 1.455 V vs. RHE for over 24 h, respectively, indicating high durability (Fig. 5c).

As shown in Fig. 5d, the OER process can be completed over the adsorption/desorption of reaction intermediates on the catalyst surface to produce O₂ [16,44,50]. Generally, the defect-rich ultrathin features and Ni sites can improve the kinetics for OH* transformation to O* and ensure fast O₂ desorption; due to these factors, the bare NiMo₃S₄ and N-NiMo₃S₄ systems possessed enriched OER activity compared to MoS₂,

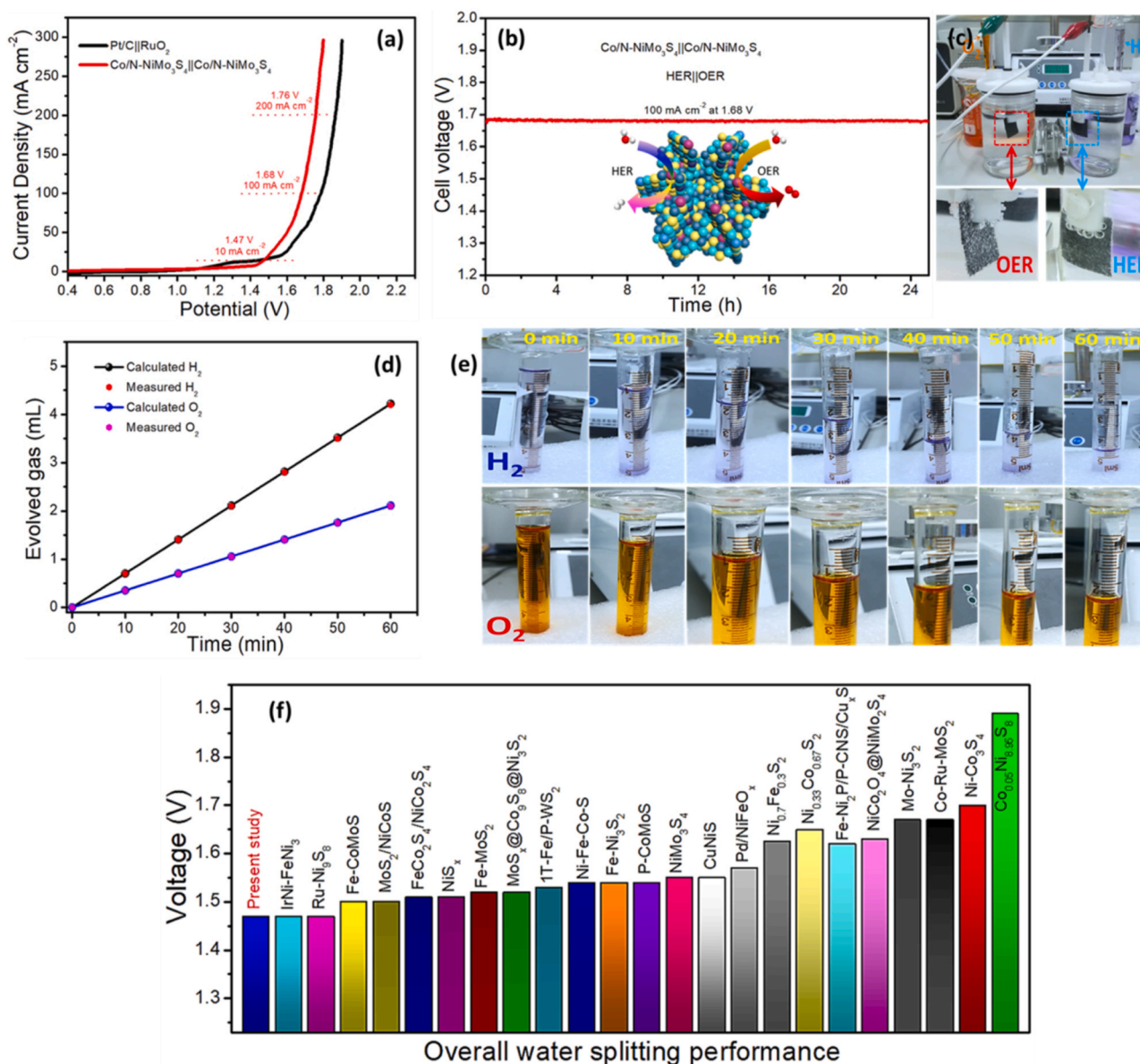


Fig. 6. (a) Overall water splitting performance of Co/N-NiMo₃S₄||Co/N-NiMo₃S₄ and Pt/C||RuO₂ electrolyzer in 1.0 M KOH solution with a two-electrode configuration. (b) Chronoamperometry curve of Co/N-NiMo₃S₄||Co/N-NiMo₃S₄ electrolyzer at a current density of 100 mA cm⁻² at a cell voltage of 1.68 V. (c) Photographic image of air-tight H-type two electrode for overall bifunctional HER and OER evolution setup. (d) Measured and calculated H₂ and O₂ gas from Co/N-NiMo₃S₄||Co/N-NiMo₃S₄ electrolyzer and their corresponding pictures. (e) Comparison of the cell voltage of Co/N-NiMo₃S₄||Co/N-NiMo₃S₄ electrolyzer with recently reported bifunctional electrocatalysts at a current density of 10 mA cm⁻².

and N-MoS₂. However, after doping with a metal (M = Co, Fe, and Cu), the enrichment in the double-layer capacitance could afford a larger electrochemical active surface area to expose a greater number of electrochemical active sites (Fig. S23). This signifies that the metal dopant (M = Co, Fe, and Cu) at nearby edge Ni active sites may simultaneously result in a moderate energy barrier for *OH, *O, and *OOH reaction intermediates [16,50]. The surface electronic structures are directly interconnected to the adsorption/desorption properties of surface active sites and the electronic structure of bare NiMo₃S₄ can be efficiently regulated by the dopant (M = Co, Fe, and Cu) atoms, while N could be an impurity center that results in a lattice strain. As a consequence, the TOF of the OER electrocatalysts at an overpotential of 220 mV is in the order of Co/N-NiMo₃S₄ (27.7 s⁻¹) > Fe/N-NiMo₃S₄ (12.1 s⁻¹) > Cu/N-NiMo₃S₄ (1.1 s⁻¹) > N-NiMo₃S₄ (0.42 s⁻¹) > NiMo₃S₄ (0.24 s⁻¹), highlighting the robust OER activity of the Co/N-NiMo₃S₄ electrocatalyst (Fig. S26). Owing to these excellent features, the OER performance of Co/N-NiMo₃S₄ is comparable and higher than previously reported robust catalysts (Fig. 5e and Table S3) [13,16,24,67,68].

3.3.3. Overall water splitting performance

To realize the potential for practical application, the Co/N-NiMo₃S₄ was employed as a cathode and anode in a two-electrode electrolyzer system for overall water splitting. Impressively, an excellent electrocatalytic performance was achieved for Co/N-NiMo₃S₄||Co/N-NiMo₃S₄ with an ultralow cell voltage of 1.47, 1.68, and 1.76 V at 10, 100, and 200 mA cm⁻² in 1.0 M KOH solution, respectively (Fig. 6a). Moreover, to validate any nanosize effects, as shown in Figs. S27-S28, a Co/NiMo₃S₄ was prepared, and due to the immature nature of the nanosheets and inadequate exposed active sites, it required higher voltages of 1.69, 2.01, and 2.13 V to reach a current density of 10, 100 and 200 mA cm⁻², respectively. In addition, the overall water splitting performance of Co/N-NiMo₃S₄||Co/N-NiMo₃S₄ outperformed Fe/N-NiMo₃S₄||Fe/N-NiMo₃S₄ (1.57, 1.81, and 1.86 V) and Pt/C||RuO₂ electrolyzer (1.46, 1.79 and 1.87 V) at 10, 100 and 200 mA cm⁻²; see Fig. 6a and Fig. S28[16,49]. To the best of our knowledge, the ultrathin

Co/N-NiMo₃S₄ Chevrel-phase is highly comparable and by far the lowest cell voltage reported for an alkaline water electrolyzer using non-noble materials. The electrolyzer's durability is another vital factor to evaluate its performance and to characterize the operational stability a chronoamperometric test was performed at a large current density of 100 mA cm⁻² at a cell voltage of 1.68 V over 24 h, this signifies that the Co/N-NiMo₃S₄||Co/N-NiMo₃S₄ electrolyzer can maintain the excellent electrocatalytic activity without obvious degradation in an alkaline solution for a prolonged time period (Fig. 6b and Fig. S29). Then, for real-world application, the amount of H₂ and O₂ evolution was measured by a drainage method in comparison with theoretical quantity to indicate the promising HER and OER Faradaic efficiencies of 99.5 ± 0.2% towards real water splitting into H₂ and O₂ and the stoichiometric ratio of generated H₂ and O₂ gases is of ~1:2, as shown Fig. 6(c-e) and Fig. S30.

The microscopic image and XPS obtained after the catalytic reaction showed a minor rupture in the morphology of Co/N-NiMo₃S₄ catalyst during water electrolysis (Fig. 7a). However, as shown in Fig. 7(b-f), an emerging of new XPS core-level peaks at 863.89 eV for Ni2p (Figs. 7b) and 773.89 and 780.35 eV for Co2p (Fig. 7e) after catalytic measurement are good agreement with NiOOH and CoOOH respectively, signifying the *in-situ* formation of Ni/Co-OOH bond through the partial oxidation of catalyst surface[57]. In addition, augmentation of 169.45 eV peak after the catalytic reaction, representing the dissolution of a small number of sulfides into the electrolyte and the partial formation of sulfate during the catalytic reaction, respectively.[30] These results clearly indicate that the *in-situ* formed Ni/CoOOH on the Co/N-NiMo₃S₄ surface could act as the real active species for overall water splitting.[57] Based on the above-mentioned analysis, the synergistic coupling of Co atoms at nearby Ni edges, defects, and the ultrathin nanosheet morphology effects upon Co/N-NiMo₃S₄ can optimize the exposed catalytic active sites and charge/mass transfer rates to increase the performance. As a result, the overall water splitting performance of the Co/N-NiMo₃S₄||Co/N-NiMo₃S₄ electrolyzer outperforms several previously reported non-precious metals based electrolyzers; see Fig. 6f and Table S4 [3,29,68].

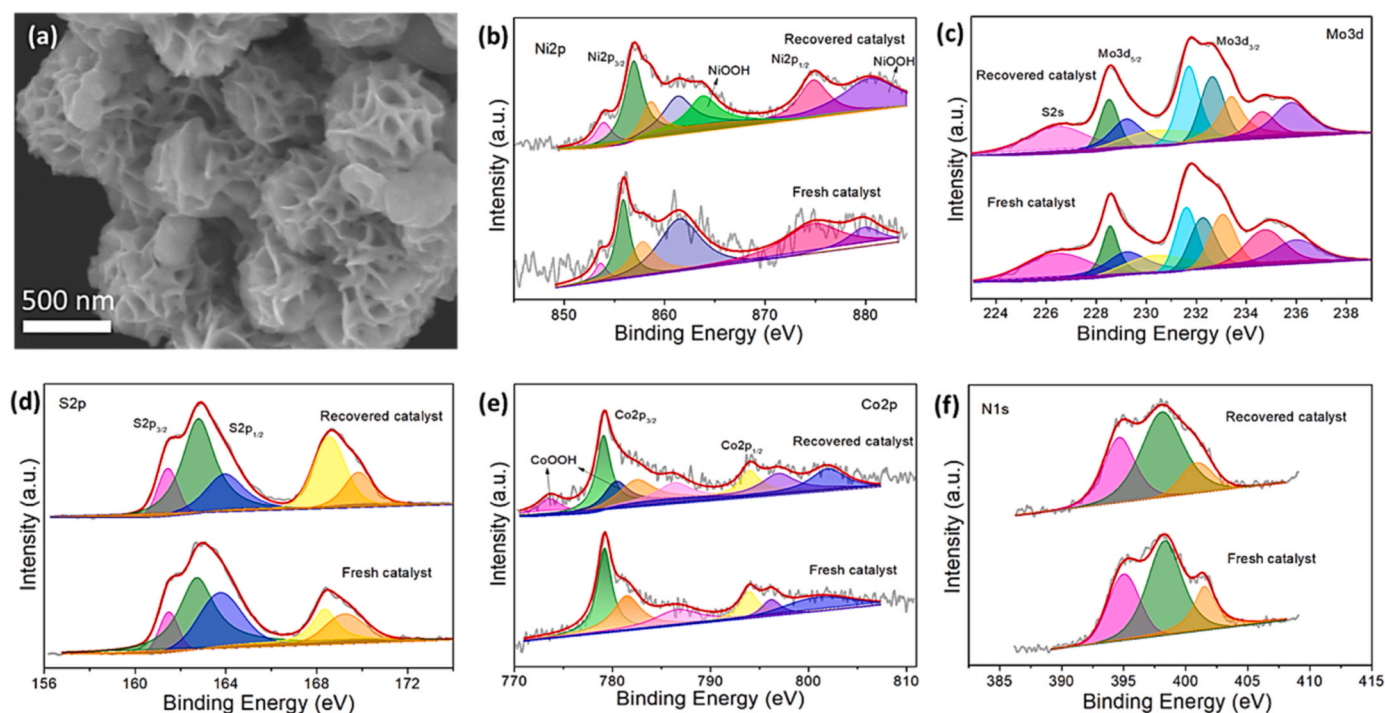


Fig. 7. (a) FE-SEM image of Co/N-NiMo₃S₄ catalyst after OER reaction and (b-f) XPS core-level spectra of fresh and recovered Co/N-NiMo₃S₄ catalyst after OER reaction.

3.4. Origin of HER/OER activities by first-principle calculations

To understand the relationship between the electronic and atomic structures and their impact on the intrinsic bifunctional HER/OER catalytic activity of NiMo_3S_4 , $\text{N-NiMo}_3\text{S}_4$, $\text{M/N-NiMo}_3\text{S}_4$ density functional theory calculations were performed (Figs. S31-S34 and Fig. 8). For alkaline HER two main continuous steps are H_2O dissociation and hydrogen adsorption (H_{ads}). From an electro-kinetic viewpoint, the

dissociation of the H_2O process may introduce an additional energy barrier and govern the overall reaction rate. Thus, the activation energy barrier of H_2O dissociation plays a significant role in determining the overall alkaline HER kinetic rate. As shown in Fig. 8(a-c), it is observed that the active Co sites that are located on edges and are under-coordinated with Ni of the $\text{Co/N-NiMo}_3\text{S}_4$ catalyst display a smaller energy barrier (0.253 eV) for decomposition of water compared to $\text{Fe/N-NiMo}_3\text{S}_4$ (0.269 eV), $\text{Cu/N-NiMo}_3\text{S}_4$ (0.313 eV), $\text{N-NiMo}_3\text{S}_4$ (0.761 eV),

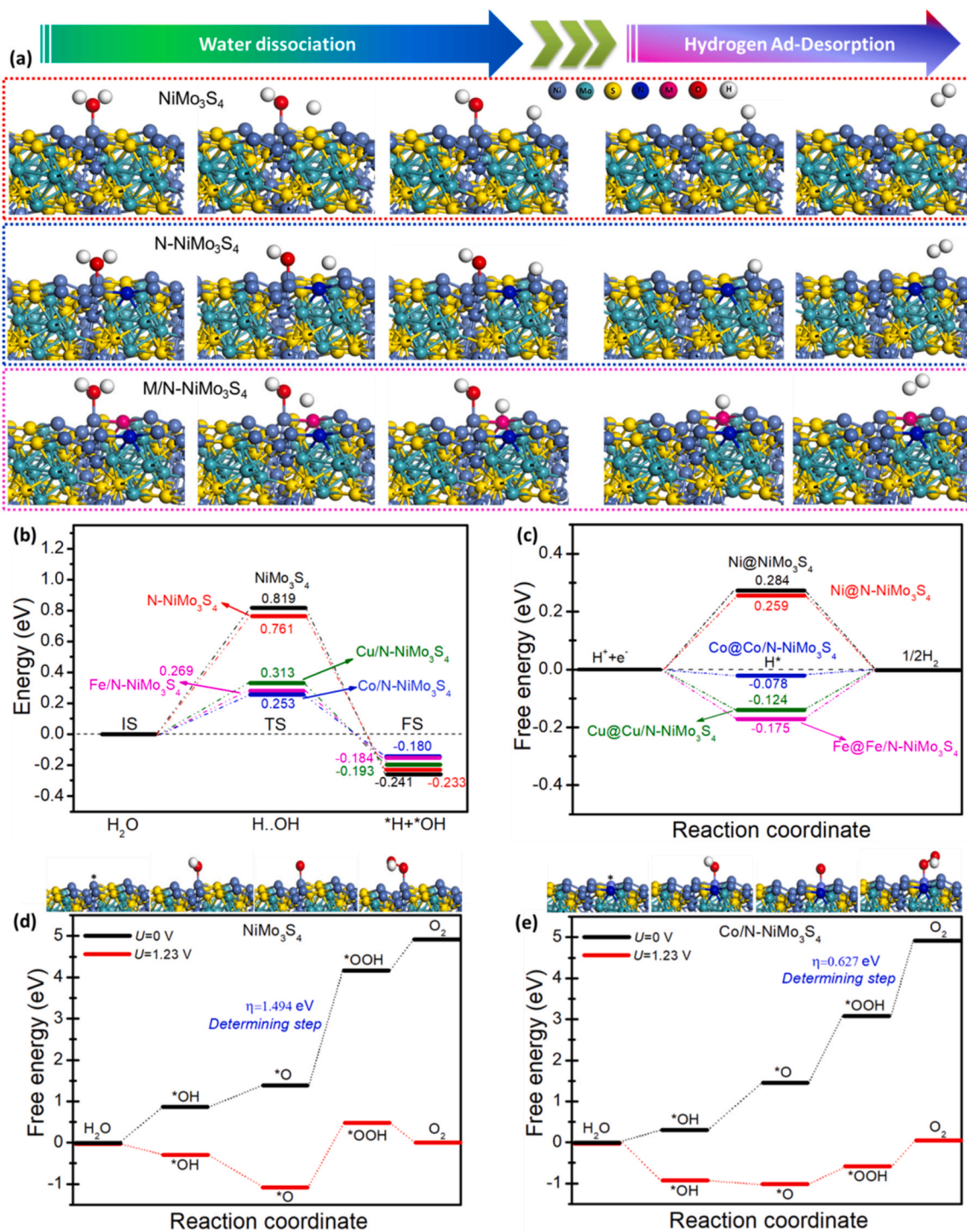


Fig. 8. (a) Chemisorption atomic models with of H_2O , H, and OH intermediates on the surfaces of NiMo_3S_4 , $\text{N-NiMo}_3\text{S}_4$, and $\text{M/N-NiMo}_3\text{S}_4$ (M = Co, Fe, and Cu) with atomic models. (b) Calculated adsorption energy diagram of the water dissociation steps and (c) Gibbs free energy diagram for all Chevrel-phased catalysts prepared in the present study. Chemisorption atomic models with OH, O, and OOH adsorption configurations and free energies for OER on the surface of (d) NiMo_3S_4 , and (e) $\text{Co/N-NiMo}_3\text{S}_4$.

and NiMo_3S_4 (0.819 eV). As a result, the $\text{Co/N-NiMo}_3\text{S}_4$ catalyst accelerates water dissociation to produce H_2 with a smaller energy barrier for alkaline HER. In addition, the Gibbs free energy of hydrogen adsorption (ΔG_{H}^*) is a key descriptor for evaluating the performance for the HER. The Co dopant site of $\text{Co/N-NiMo}_3\text{S}_4$ exhibits a much lower ΔG_{H}^* (−0.078 eV) relative to the $\text{Fe/N-NiMo}_3\text{S}_4$ (−0.175 eV), $\text{Cu/N-NiMo}_3\text{S}_4$ (−0.124 eV), $\text{N-NiMo}_3\text{S}_4$ (0.259 eV) and NiMo_3S_4 (0.284 eV); this indicates that an optimal amount of metal dopants ($\text{M} = \text{Co}, \text{Fe}, \text{and Cu}$) at edges of nearby Ni atoms can facilitate favorable H^* adsorption and lead to a reduction of the thermodynamic barriers for H_2 generation (Fig. S35). Notably, as shown in Fig. 8(b–c), the corresponding reaction pathway of the $\text{Co/N-NiMo}_3\text{S}_4$ catalyst has a relatively high energy barrier for the Volmer step (0.253 eV) and a low hydrogen adsorption free energy (−0.078 eV), indicating a Volmer–Heyrovsky pathway. This result is in agreement with the measured Tafel slope of $\text{Co/N-NiMo}_3\text{S}_4$ catalyst for HER (69 mV dec^{-1} ; Fig. 4c), further highlighting the Volmer–Heyrovsky mechanism [1,39,46]. Hypothetically, alkaline water oxidation involves four concerted proton-electron transfer steps. Fig. 8(d–e) and Figs. S36–S40 show the configuration of the reaction intermediates and calculated OER energy profiles for different exposed atomic sites of prepared the Chevrel-phases of the $\text{Co/N-NiMo}_3\text{S}_4$, $\text{Fe/N-NiMo}_3\text{S}_4$, $\text{Cu/N-NiMo}_3\text{S}_4$, $\text{N-NiMo}_3\text{S}_4$ and NiMo_3S_4 electrocatalysts. Noticeably, the potential rate-determining step (PDS) of NiMo_3S_4 is the third electrochemical reaction step from $^*\text{O}$ to $^*\text{OOH}$, with an energy barrier of 1.49 eV. Conversely, the species of $^*\text{OOH}$ on $\text{Co/N-NiMo}_3\text{S}_4$ is significantly improved, and the overpotential is reduced to 0.67 V with the PDS of creating an O_2 molecule, which reveals a more thermodynamically favorable OER process. Firstly, the $^*\text{OH}$ species will be formed on the active metal Co site and provides one proton to the system. Then, a single oxygen atom will be adsorbed onto the Co site and react with H_2O through a nucleophilic attack, while the $^*\text{OOH}$ will be formed by deprotonation. The formation of $^*\text{OOH}$ would be the PDS during the OER process. Finally, proton-coupled electron transfer facilitates the efficient release of O_2 [16,44,50]. It is also observed that the metal dopants in $\text{Fe/N-NiMo}_3\text{S}_4$ and $\text{Cu/N-NiMo}_3\text{S}_4$ can reduce the energy barrier while, due to the nanosheet features, the $\text{N-NiMo}_3\text{S}_4$ has a small influence on the decrease of the energy barrier compared to bare NiMo_3S_4 (i.e., N could be impurity center and not an active site in $\text{N-NiMo}_3\text{S}_4$). These results signify that an optimal number of Co atoms which coupled with nearby active Ni edge sites in a NiMo_3S_4 Chevrel-phase of a 2D morphology are crucial for the constructive stabilization of reaction intermediates and superior electrochemical kinetics, compared to the use of Fe and Cu dopants.

In order to evaluate the enrichment of 3d electrons for all Chevrel-phase samples, charge density plots were determined and are shown in Fig. 1, and Figs. S41–S42. Remarkably, the charge density difference plots indicate enhanced orbital hybridization between the Co and Ni atoms in the $\text{Co/N-NiMo}_3\text{S}_4$, which results in enriched electron transfer than NiMo_3S_4 (Fig. 1(e–f)). By virtue of its low electronegativity, the optimal amount of Co atoms can induce a delocalization of d-electrons, which increases the charge density in the $\text{Co/N-NiMo}_3\text{S}_4$; it can also facilitate fast electron transfer during the electrocatalytic process. In addition, this result indicates that after Co incorporation, the electrons and their spin states in the $\text{Co/N-NiMo}_3\text{S}_4$ are more delocalized than NiMo_3S_4 , $\text{N-NiMo}_3\text{S}_4$, $\text{Fe/N-NiMo}_3\text{S}_4$, and $\text{Cu/N-NiMo}_3\text{S}_4$; as a result, the d-electrons enriched (Fig. 1(d–f), and Figs. S41–S42). To gain an insight into the distribution of 3d electrons, the density of states (DOS) and projected density of states (PDOS) of the d orbitals are subsequently calculated and shown in Fig. 1d and Figs. S43–S44. It can be seen in Fig. 1d and Fig. S44 that there is an increased DOS for the unoccupied states from ≈ 0.50 eV to the Fermi level with respect to the bare NiMo_3S_4 ; this could be due to the delocalized electrons that are induced by metal cation incorporation [49,56]. Compared to all other catalysts examined, $\text{Co/N-NiMo}_3\text{S}_4$ showed an increased density of states (DOS), and the enrichment of electron density around the Ni atoms is induced by the presence of Co compared to Fe and Cu. This observation

demonstrates that the Co dopant efficiently optimized the electron state of the nearby edge Ni atoms in the $\text{Co/N-NiMo}_3\text{S}_4$, thereby improving electrocatalytic activity. As shown in Fig. S44, the PDOS on d orbitals are calculated, where it can upshift the d-band center of $\text{Co/N-NiMo}_3\text{S}_4$, thereby decreasing the energy barrier for the formation of $^*\text{OOH}$ on the Co site neighbouring to the Ni edge site and facilitating a robust HER and OER process [42,49,56]. Overall, the DFT simulations and experimental results demonstrate that the outstanding HER and OER activities are facilitated by the presence of delocalized d-electrons that are induced by Co atoms at the edges of the Ni sites, which accelerates rapid electron transfer during the electrocatalytic process. This indicates that in a $\text{Co/N-NiMo}_3\text{S}_4$ Chevrel-phase, the presence of Co and Ni atoms at an optimal content is crucial to realize robust alkaline water splitting through d-electron delocalization. In addition, the interconnected $[\text{Mo}_6\text{S}_8]^{2-}$ cluster units in the $\text{Co/N-NiMo}_3\text{S}_4$ allow faster charge transfer kinetics and the N could be an impurity center, thereby facilitating the robust electrocatalytic bifunctional water splitting process.

4. Conclusion

In summary, we propose a pioneering strategy to create robust and high performance bifunctional electrocatalysts using the delocalization of d-electrons by the incorporation of metal cations in self-assembled and ultrathin nanosheets of a $\text{M/N-NiMo}_3\text{S}_4$ ($\text{M} = \text{Co}, \text{Fe}$ and Cu) Chevrel-phase. Remarkably, the hydrogen evolution reaction (HER) and oxygen evolution reaction (OER) performance of $\text{Co/N-NiMo}_3\text{S}_4$ is higher than other prepared samples and previously reported robust catalysts. Specifically, the $\text{Co/N-NiMo}_3\text{S}_4$ Chevrel-phase displays remarkable electrocatalytic performance for both the HER and OER, which requires low overpotentials of 78, 208, 282, and 307 mV to provide current densities of 10, 100, 500, and 1000 mA cm^{-2} for the HER; and for OER, 186, 204, and 225 mV, at 50, 100, and 300 mA cm^{-2} , respectively. In addition, the assembled $\text{Co/N-NiMo}_3\text{S}_4 \parallel \text{Co/N-NiMo}_3\text{S}_4$ electrolyzer achieved an ultralow cell voltage of 1.47, 1.68, and 1.76 V at 10, 100, and 200 mA cm^{-2} and was able to maintain operational stability for over 24 h. As a result, the overall water splitting performance of the $\text{Co/N-NiMo}_3\text{S}_4 \parallel \text{Co/N-NiMo}_3\text{S}_4$ electrolyzer outperforms several previously reported non-precious metals based electrolyzers. A combination of detailed experimental and density functional theory (DFT) calculations have provided new insights on intrinsic kinetic mechanisms associated with the electrocatalytic bifunctional hydrogen and oxygen evolution reactions; (i) ultrathin nanosheets of the $\text{Co/N-NiMo}_3\text{S}_4$ Chevrel-phase electrocatalyst are formed with well-defined reaction edge sites for bifunctional HER/OER to overcome the steric hindrance of reaction intermediates for water adsorption/dissociation; (ii) by virtue of its low electronegativity, an optimal amount of Co atoms are coupled with nearby Ni edge atoms to facilitate charge transfer and enhance the catalytic properties of $\text{Co/N-NiMo}_3\text{S}_4$ nanosheets through enrichment of the d-electron density; (iii) the charge density plots indicate an enhanced orbital hybridization between the Co and Ni atoms in the $\text{Co/N-NiMo}_3\text{S}_4$, which results in an enriched electron transfer than all other samples, signifying an efficient charge transfer to improve overall water electrolysis; (iv) the upshift in d-band center of the $\text{Co/N-NiMo}_3\text{S}_4$ phase can optimize the free energies of a variety of reaction intermediates such as H^* , OH^* , O^* , OOH^* for water adsorption/dissociation, thereby facilitating robust alkaline water electrolysis; (v) the interconnected $[\text{Mo}_6\text{S}_8]^{2-}$ cluster units in the $\text{Co/N-NiMo}_3\text{S}_4$ provides improved charge transfer kinetics, while the N could be a impurity center in the $\text{Co/N-NiMo}_3\text{S}_4$; (vi) the ultrathin nature of the $\text{Co/N-NiMo}_3\text{S}_4$ nanosheets, combined with its defective features and large surface area can improve the electron/mass transport and increase the number of exposed edge active sites to facilitate rapid alkaline HER/OER. As a result of these intrinsic benefits, the $\text{Co/N-NiMo}_3\text{S}_4$ exhibits excellent electrocatalytic water splitting performance and outstanding stability in alkaline media, making it a highly promising electrocatalyst for large-current water electrolysis. We believe that the designed

Chevrete-phase electrocatalysts, which benefit from the d-electron delocalization strategy, can shed new light on the design of advanced energy materials for electrocatalysis and other energy conversion/storage applications.

CRediT authorship contribution statement

Sundaram Chandrasekaran: Conceptualization, Investigation, Data curation, Software, Writing – original draft, Funding acquisition. **Tingting Ma:** Investigation, Methodology, Data curation, Software. **Zhichang Hu:** Visualization, Software. **Qianying Liu:** Data curation and Software. **Chao Zhan:** Methodology, Validation. **Yan Li:** Data curation, Validation. **Chris Bowen:** Validation, Writing – review & editing. **Huidan Lu:** Project administration, Validation, Supervision, Funding acquisition. **Yongping Liu:** Validation, Writing – review & editing. Project administration, Funding acquisition, Supervision.

Declaration of Competing Interest

The authors declare the following financial interests/personal relationships which may be considered as potential competing interests: Sundaram Chandrasekaran reports financial support was provided by National Natural Science Foundation of China. Yongping Liu reports financial support was provided by National Natural Science Foundation of China. Sundaram Chandrasekaran reports financial support was provided by Guangxi Science and Technology Fund for Distinguished High-Talent Introduction Program. Yongping Liu reports financial support was provided by Guangxi Science Fund for Distinguished Young Scholars.

Data Availability

Data will be made available on request.

Acknowledgments

This work was supported by the National Natural Science Foundation of China (22262010, 22062005, 22165005, U20A20128), Guangxi Science and Technology Fund for Distinguished High-Talent Introduction Program (AC22035091), Guangxi Science Fund for Distinguished Young Scholars (2019GXNSFFA245016), and the Scientific Research Start-Up Project Program of the Guilin University of Technology (2000002183), Guilin, PR China.

Appendix A. Supporting information

Supplementary data associated with this article can be found in the online version at doi:10.1016/j.apcatb.2023.123007.

References

- [1] Y. Wang, X. Li, M. Zhang, J. Zhang, Z. Chen, X. Zheng, Z. Tian, N. Zhao, X. Han, K. Zaghib, Y. Wang, Y. Deng, W. Hu, Highly active and durable single-atom tungsten-doped $\text{NiS}_{0.5}\text{Se}_{0.5}$ nanosheet @ $\text{NiS}_{0.5}\text{Se}_{0.5}$ nanorod heterostructures for water splitting, *Adv. Mater.* 34 (2022) 2107053.
- [2] S. Chandrasekaran, D. Ma, Y. Ge, L. Deng, C. Bowen, J. Roscow, Y. Zhang, Z. Lin, R. D.K. Misra, J. Li, P. Zhang, H. Zhang, Electronic structure engineering on two-dimensional (2D) electrocatalytic materials for oxygen reduction, oxygen evolution, and hydrogen evolution reactions, *Nano Energy* 77 (2020), 105080.
- [3] S. Ramakrishnan, D.B. Velusamy, S. Sengodan, G. Nagaraju, D.H. Kim, A.R. Kim, D. J. Yoo, Rational design of multifunctional electrocatalyst: an approach towards efficient overall water splitting and rechargeable flexible solid-state zinc–air battery, *Appl. Catal. B: Environ.* 300 (2022), 120752.
- [4] Y. Luo, Z. Zhang, M. Chhowalla, B. Liu, Recent advances in design of electrocatalysts for high-current-density water splitting, *Adv. Mater.* 34 (2022) 2108133.
- [5] J.-T. Ren, L. Chen, H.-Y. Wang, W.-W. Tian, X. Zhang, T.-Y. Ma, Z. Zhou, Z.-Y. Yuan, Inducing electronic asymmetry on Ru clusters to boost key reaction steps in basic hydrogen evolution, *Appl. Catal. B: Environ.* 327 (2023), 122466.
- [6] W. Yu, Z. Chen, Y. Fu, W. Xiao, T. Ma, B. Dong, Y. Chai, Z. Wu, L. Wang, Co-Mo microcolumns decorated with trace Pt for large current density hydrogen generation in alkaline seawater, *Appl. Catal. B: Environ.* 317 (2022), 121762.
- [7] Z. Wu, Y. Zhao, W. Xiao, Y. Fu, B. Jia, T. Ma, L. Wang, Metallic-bonded Pt-Co for atomically dispersed Pt in the Co_4N matrix as an efficient electrocatalyst for hydrogen generation, *ACS Nano* 16 (2022) 18038–18047.
- [8] C. Huang, L. Yu, W. Zhang, Q. Xiao, J. Zhou, Y. Zhang, P. An, J. Zhang, Y. Yu, N-doped Ni-Mo based sulfides for high-efficiency and stable hydrogen evolution reaction, *Appl. Catal. B: Environ.* 276 (2020), 119137.
- [9] J. Miao, F.-X. Xiao, H.B. Yang, S.Y. Khoo, J. Chen, Z. Fan, Y.-Y. Hsu, H.M. Chen, H. Zhang, B. Liu, Hierarchical Ni-Mo-S nanosheets on carbon fiber cloth: a flexible electrode for efficient hydrogen generation in neutral electrolyte, *Sci. Adv.* 1 (2015), e1500259.
- [10] S. Chandrasekaran, L. Yao, L. Deng, C. Bowen, Y. Zhang, S. Chen, Z. Lin, F. Peng, P. Zhang, Recent advances in metal sulfides: from controlled fabrication to electrocatalytic, photocatalytic and photoelectrochemical water splitting and beyond, *Chem. Soc. Rev.* 48 (2019) 4178–4280.
- [11] J. Staszak-Jirkovský, Christos D. Malliakas, Pietro P. Lopes, N. Danilovic, Subrahmanyam S. Kota, K.-C. Chang, B. Genorio, D. Strmcnik, Vojislav R. Stamenkovic, M.G. Kanatzidis, N.M. Markovic, Design of active and stable Co–Mo–S_x chalcogenides as pH-universal catalysts for the hydrogen evolution reaction, *Nat. Mater.* 15 (2016) 197–203.
- [12] G.W. Huber, J.W. Shabaker, J.A. Dumesic, Raney Ni-Sn catalyst for H₂ production from biomass-derived hydrocarbons, *Science* 300 (2003) 2075–2077.
- [13] M. Wang, L. Zhang, Y. He, H. Zhu, Recent advances in transition-metal-sulfide-based bifunctional electrocatalysts for overall water splitting, *J. Mater. Chem. A* 9 (2021) 5320–5363.
- [14] T. Zhu, L. Zhu, J. Wang, G.W. Ho, In situ chemical etching of tunable 3D Ni_3S_2 superstructures for bifunctional electrocatalysts for overall water splitting, *J. Mater. Chem. A* 4 (2016) 13916–13922.
- [15] W. He, F. Wang, Y. Gao, Q. Hao, C. Liu, One-step synthesis of amorphous transition metal sulfides as bifunctional electrocatalysts for the hydrogen evolution reaction and oxygen evolution reaction, *Sustain. Energy Fuels* 6 (2022) 3852–3857.
- [16] Q. Gao, W. Luo, X. Ma, Z. Ma, S. Li, F. Gou, W. Shen, Y. Jiang, R. He, M. Li, Electronic modulation and vacancy engineering of Ni_9S_8 to synergistically boost efficient water splitting: active vacancy-metal pairs, *Appl. Catal. B: Environ.* 310 (2022), 121356.
- [17] J.-Y. Xue, F.-L. Li, Z.-Y. Zhao, C. Li, C.-Y. Ni, H.-W. Gu, D.J. Young, J.-P. Lang, In situ generation of bifunctional Fe-Doped MoS_2 nanocapillaries for efficient electrocatalytic water splitting, *Inorg. Chem.* 58 (2019) 11202–11209.
- [18] G. Zhang, Y.-S. Feng, W.-T. Lu, D. He, C.-Y. Wang, Y.-K. Li, X.-Y. Wang, F.-F. Cao, Enhanced catalysis of electrochemical overall water splitting in alkaline media by Fe doping in Ni_3S_2 nanosheet arrays, *ACS Catal.* 8 (2018) 5431–5441.
- [19] J. Chen, L. Zhang, J. Li, X. He, Y. Zheng, S. Sun, X. Fang, D. Zheng, Y. Luo, Y. Wang, J. Zhang, L. Xie, Z. Cai, Y. Sun, A.A. Alshehri, Q. Kong, C. Tang, X. Sun, High-efficiency overall alkaline seawater splitting: using a nickel–iron sulfide nanosheet array as a bifunctional electrocatalyst, *J. Mater. Chem. A* 11 (2023) 1116–1122.
- [20] D. Zheng, Z. Jing, Q. Zhao, Y. Kim, P. Li, H. Xu, Z. Li, J. Lin, Efficient Co-doped pyrrhotite $\text{Fe}_{0.95}\text{S}_{1.05}$ nanoplates for electrochemical water splitting, *Chem. Eng. J.* 402 (2020), 125069.
- [21] D. Liu, Q. Lu, Y. Luo, X. Sun, A.M. Asiri, NiCo_2S_4 nanowires array as an efficient bifunctional electrocatalyst for full water splitting with superior activity, *Nanoscale* 7 (2015) 15122–15126.
- [22] Z. Peng, D. Jia, A.M. Al-Enizi, A.A. Elzatahry, G. Zheng, From water oxidation to reduction: homologous Ni–Co based nanowires as complementary water splitting electrocatalysts, *Adv. Energy Mater.* 5 (2015) 1402031.
- [23] C. Ray, S.C. Lee, K.V. Sankar, B. Jin, J. Lee, J.H. Park, S.C. Jun, Amorphous phosphorus-incorporated cobalt molybdenum sulfide on carbon cloth: an efficient and stable electrocatalyst for enhanced overall water splitting over entire pH Values, *ACS Appl. Mater. Interfaces* 9 (2017) 37739–37749.
- [24] Y. Guo, X. Zhou, J. Tang, S. Tanaka, Y.V. Kaneti, J. Na, B. Jiang, Y. Yamauchi, Y. Bando, Y. Sugahara, Multiscale structural optimization: highly efficient hollow iron-doped metal sulfide heterostructures as bifunctional electrocatalysts for water splitting, *Nano Energy* 75 (2020), 104913.
- [25] J. Guo, X. Zhang, Y. Sun, L. Tang, X. Zhang, Self-template synthesis of hierarchical CoMoS_3 nanotubes constructed of ultrathin nanosheets for robust water electrolysis, *J. Mater. Chem. A* 5 (2017) 11309–11315.
- [26] D. Kong, Y. Wang, S. Huang, Y.V. Lim, M. Wang, T. Xu, J. Zang, X. Li, H.Y. Yang, Defect-engineered 3D hierarchical NiMo_3S_4 nanoflowers as bifunctional electrocatalyst for overall water splitting, *J. Colloid Interface Sci.* 607 (2022) 1876–1887.
- [27] G. Barati Darband, M. Aliofkhazraei, S. Hyun, A. Sabour Rouhaghdam, S. Shanmugam, Electrodeposition of Ni–Co–Fe mixed sulfide ultrathin nanosheets on Ni nanorods: a low-cost, durable and high performance catalyst for electrochemical water splitting, *Nanoscale* 11 (2019) 16621–16634.
- [28] K. Li, D. Feng, Y. Tong, Hierarchical metal sulfides heterostructure as superior bifunctional electrode for overall water splitting, *ChemSusChem* 15 (2022), e202200590.
- [29] S. Ramakrishnan, J. Balamurugan, M. Vinothkannan, A.R. Kim, S. Sengodan, D. J. Yoo, Nitrogen-doped graphene encapsulated FeCoMoS nanoparticles as advanced trifunctional catalyst for water splitting devices and zinc–air batteries, *Appl. Catal. B: Environ.* 279 (2020), 119381.
- [30] J. Jiang, M. Gao, W. Sheng, Y. Yan, Hollow chevrete-phase NiMo_3S_4 for hydrogen evolution in alkaline electrolytes, *Angew. Chem. Int. Ed.* 55 (2016) 15240–15245.
- [31] K. Yvon, A. Paoli, Charge transfer and valence electron concentration in Chevrete phases, *Solid State Commun.* 24 (1977) 41–45.

- [32] N. Alonso-Vante, Introduction, Chalcogenide Materials for Energy Conversion: Pathways to Oxygen and Hydrogen Reactions, Springer International Publishing, Cham, 2018, pp. 1–25.
- [33] J. Guillelme, M.O. Bars, D. Grandjean, Etude structurale de combinaisons sulfurées et sélénées du molybdène. III. Structure cristalline de NiMo_3S_4 , *J. Solid State Chem.* 7 (1973) 158–162.
- [34] J. Guillelme, O. Bars, D. Grandjean, Etude structurale de combinaisons sulfurées et sélénées du molybdène. V. Structures cristallines de phases $\text{M}_3\text{Mo}_3\text{S}_4$ ($\text{M} = \text{Ni}, \text{Co}, \text{Fe}$), *Acta Crystallogr. B. Struct. Cryst.* 32 (1976) 1338–1342.
- [35] R. Chevrel, M. Sergent, J. Prigent, Sur de nouvelles phases sulfurées ternaires du molybdène, *J. Solid State Chem.* 3 (1971) 515–519.
- [36] K.F. McCarty, J.W. Anderegg, G.L. Schrader, Hydrodesulfurization catalysis by Chevrel phase compounds, *J. Catal.* 93 (1985) 375–387.
- [37] M. Mao, Z. Lin, Y. Tong, J. Yue, C. Zhao, J. Lu, Q. Zhang, L. Gu, L. Suo, Y.-S. Hu, H. Li, X. Huang, L. Chen, Iodine vapor transport-triggered preferential growth of chevrel Mo_6S_8 nanosheets for advanced multivalent batteries, *ACS Nano*. 14 (2020) 1102–1110.
- [38] R. Chevrel, M. Hirrien, M. Sergent, Superconducting Chevrel phases: prospects and perspectives, *Polyhedron* 5 (1986) 87–94.
- [39] D. Kong, Y. Wang, Y.V. Lim, S. Huang, J. Zhang, B. Liu, T. Chen, H.Y. Yang, 3D hierarchical defect-rich NiMo_3S_4 nanosheet arrays grown on carbon textiles for high-performance sodium-ion batteries and hydrogen evolution reaction, *Nano Energy* 49 (2018) 460–470.
- [40] W. Jaegermann, C. Pettenkofer, N. Alonso Vante, T. Schwarzlose, H. Tributsch, Chevrel phase type compounds: electronic, chemical and structural factors in oxygen reduction electrocatalysis, *Ber. der Bunsenges. für Phys. Chem.* 94 (1990) 513–520.
- [41] S. Chandrasekaran, M. Khandelwal, F. Dayong, L. Sui, J.S. Chung, R.D.K. Misra, P. Yin, E.J. Kim, W. Kim, A. Vanchiappan, Y. Liu, S.H. Hur, H. Zhang, C. Bowen, Developments and perspectives on robust nano- and microstructured binder-free electrodes for bifunctional water electrolysis and beyond, *Adv. Energy Mater.* 12 (2022) 2200409.
- [42] Q. Dai, L. Wang, K. Wang, X. Sang, Z. Li, B. Yang, J. Chen, L. Lei, L. Dai, Y. Hou, Accelerated water dissociation kinetics by electron-enriched cobalt sites for efficient alkaline hydrogen evolution, *Adv. Funct. Mater.* 32 (2022) 2109556.
- [43] J. Wang, Z. Zhang, H. Song, B. Zhang, J. Liu, X. Shai, L. Miao, Water dissociation kinetic-oriented design of nickel sulfides via tailored dual sites for efficient alkaline hydrogen evolution, *Adv. Funct. Mater.* 31 (2021) 2008578.
- [44] Y. Huang, L.-W. Jiang, B.-Y. Shi, K.M. Ryan, J.-J. Wang, Highly efficient oxygen evolution reaction enabled by phosphorus doping of the Fe electronic structure in iron–nickel selenide nanosheets, *Adv. Sci.* 8 (2021) 2101775.
- [45] P. Zhai, Y. Zhang, Y. Wu, J. Gao, B. Zhang, S. Cao, Y. Zhang, Z. Li, L. Sun, J. Hou, Engineering active sites on hierarchical transition bimetal oxides/sulfides heterostructure array enabling robust overall water splitting, *Nat. Commun.* 11 (2020) 5462.
- [46] T. Wu, E. Song, S. Zhang, M. Luo, C. Zhao, W. Zhao, J. Liu, F. Huang, Engineering metallic heterostructure based on Ni_3N and 2M– MoS_2 for alkaline water electrolysis with industry-compatible current density and stability, *Adv. Mater.* 34 (2022) 2108505.
- [47] S. Chandrasekaran, N. Li, Y. Zhuang, L. Sui, Z. Xiao, D. Fan, V. Aravindan, C. Bowen, H. Lu, Y. Liu, Interface charge density modulation of a lamellar-like spatially separated Ni_9S_8 nanosheet/ Nb_2O_5 nanobelt heterostructure catalyst coupled with nitrogen and metal ($\text{M} = \text{Co}, \text{Fe}, \text{or Cu}$) atoms to accelerate acidic and alkaline hydrogen evolution reactions, *Chem. Eng. J.* 431 (2022), 134073.
- [48] S. Chandrasekaran, P. Zhang, F. Peng, C. Bowen, J. Huo, L. Deng, Tailoring the geometric and electronic structure of tungsten oxide with manganese or vanadium doping toward highly efficient electrochemical and photoelectrochemical water splitting, *J. Mater. Chem. A* 7 (2019) 6161–6172.
- [49] R. Zhang, Z. Wei, G. Ye, G. Chen, J. Miao, X. Zhou, X. Zhu, X. Cao, X. Sun, “d-electron complementation” induced V–Co phosphide for efficient overall water splitting, *Adv. Energy Mater.* 11 (2021) 2101758.
- [50] S. Chen, Z. Kang, X. Hu, X. Zhang, H. Wang, J. Xie, X. Zheng, W. Yan, B. Pan, Y. Xie, Delocalized spin states in 2D atomic layers realizing enhanced electrocatalytic oxygen evolution, *Adv. Mater.* 29 (2017) 1701687.
- [51] Z.D. Wang, M. Yoshida, B. George, Theoretical study on the thermal decomposition of thiourea, *Comput. Theor. Chem.* 1017 (2013) 91–98.
- [52] S. Chandrasekaran, C. Zhang, Y. Shu, H. Wang, S. Chen, T. Nesakumar Jebakumar Immanuel Edison, Y. Liu, N. Karthik, R.D.K. Misra, L. Deng, P. Yin, Y. Ge, O.A. Al-Hartomy, A. Al-Ghamdi, S. Wageh, P. Zhang, C. Bowen, Z. Han, Advanced opportunities and insights on the influence of nitrogen incorporation on the physico-/electro-chemical properties of robust electrocatalysts for electrocatalytic energy conversion, *Coord. Chem. Rev.* 449 (2021), 214209.
- [53] Q. Liu, X. Li, Q. He, A. Khalil, D. Liu, T. Xiang, X. Wu, L. Song, Gram-scale aqueous synthesis of stable few-layered 1T– MoS_2 : applications for visible-light-driven photocatalytic hydrogen evolution, *Small* 11 (2015) 5556–5564.
- [54] E. Guerrero, R. Karkee, D.A. Strubbe, Phase stability and Raman/IR signatures of Ni-doped MoS_2 from density functional theory studies, *J. Phys. Chem. C* 125 (2021) 13401–13412.
- [55] D.J. Holmgren, R.T. Demers, M.V. Klein, D.M. Ginsberg, Raman study of phonons in Chevrel-phase crystals, *Phys. Rev. B* 36 (1987) 1952–1955.
- [56] S. Shen, Z. Wang, Z. Lin, K. Song, Q. Zhang, F. Meng, L. Gu, W. Zhong, Crystalline-amorphous interfaces coupling of CoSe_2/CoP with optimized d-band center and boosted electrocatalytic hydrogen evolution, *Adv. Mater.* 34 (2022) 2110631.
- [57] H. Su, S. Song, S. Li, Y. Gao, L. Ge, W. Song, T. Ma, J. Liu, High-valent bimetal $\text{Ni}_3\text{S}_2/\text{Co}_3\text{S}_4$ induced by Cu doping for bifunctional electrocatalytic water splitting, *Appl. Catal. B: Environ.* 293 (2021), 120225.
- [58] N.A. Vante, B. Schubert, H. Tributsch, A. Perrin, Influence of d-state density and chemistry of transition metal cluster selenides on electrocatalysis, *J. Catal.* 112 (1988) 384–391.
- [59] K. Kobayashi, A. Fujimori, T. Ohtani, I. Dasgupta, O. Jepsen, O.K. Andersen, Electronic structure of the Chevrel-phase compounds $\text{Sn}_x\text{Mo}_6\text{Se}_{7.5}$: Photoemission spectroscopy and band-structure calculations, *Phys. Rev. B* 63 (2001), 195109.
- [60] E. Agostinelli, C. Battistoni, D. Fiorani, G. Mattogno, M. Nogués, An XPS study of the electronic structure of the $\text{Zn}_x\text{Cd}_{1-x}\text{Cr}_2\text{S}_4$ ($x = \text{S}, \text{Se}$) spinel system, *J. Phys. Chem. Solids* 50 (1989) 269–272.
- [61] Applications in Coordination Chemistry, Infrared and Raman Spectra of Inorganic and Coordination Compounds, 2008, pp. 1–273.
- [62] N.H. Turner, A.M. Single, Determination of peak positions and areas from wide-scan XPS spectra, *Surf. Interface Anal.* 15 (1990) 215–222.
- [63] Z. Nie, L. Zhang, X. Ding, M. Cong, F. Xu, L. Ma, M. Guo, M. Li, L. Zhang, Catalytic kinetics regulation for enhanced electrochemical nitrogen oxidation by Ru-nanoclusters-coupled Mn_3O_4 catalysts decorated with atomically dispersed Ru atoms, *Adv. Mater.* 34 (2022) 2108180.
- [64] Y. Cao, L. Guo, M. Dan, D.E. Doronkin, C. Han, Z. Rao, Y. Liu, J. Meng, Z. Huang, K. Zheng, P. Chen, F. Dong, Y. Zhou, Modulating electron density of vacancy site by single Au atom for effective CO_2 photoreduction, *Nat. Commun.* 12 (2021) 1675.
- [65] Y. Zhang, F. Du, R. Wang, X. Ling, X. Wang, Q. Shen, Y. Xiong, T. Li, Y. Zhou, Z. Zou, Electrocatalytic fixation of N_2 into NO^{3-} : electron transfer between oxygen vacancies and loaded Au in Nb_2O_5-x nanobelts to promote ambient nitrogen oxidation, *J. Mater. Chem. A* 9 (2021) 17442–17450.
- [66] R. Zhang, X. Wang, S. Yu, T. Wen, X. Zhu, F. Yang, X. Sun, X. Wang, W. Hu, Ternary NiCo_2P_x nanowires as pH-universal electrocatalysts for highly efficient hydrogen evolution reaction, *Adv. Mater.* 29 (2017) 1605502.
- [67] R. Santhosh Kumar, S.C. Karthikeyan, S. Ramakrishnan, S. Vijayapradeep, A. Rhan Kim, J.-S. Kim, D. Jin, Yoo, Anion dependency of spinel type cobalt catalysts for efficient overall water splitting in an acid medium, *Chem. Eng. J.* 451 (2023), 138471.
- [68] E. Vijayakumar, S. Ramakrishnan, C. Sathiskumar, D.J. Yoo, J. Balamurugan, H. S. Noh, D. Kwon, Y.H. Kim, H. Lee, MOF-derived CoP-nitrogen-doped carbon@NiFeP nanoflakes as an efficient and durable electrocatalyst with multiple catalytically active sites for OER, HER, ORR and rechargeable zinc-air batteries, *Chem. Eng. J.* 428 (2022), 131115.